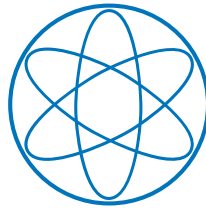Lana Rekhviashvili

Studies of Collision Operators and Applications in Tokamak Plasmas

Master Thesis in Physics at
Technische Universität München

Studies of Collision Operators and Applications in Tokamak Plasmas

presented by

Lana Rekhviashvili

27.01.2023, Munich

Supervisors:

Dr. Zhixin Lu

Dr. Matthias Hoelzl

Academic Supervisor: Dr. Philipp Lauber

Contents

Abstract

For magnetic confinement fusion in Tokamak plasma, some of the limitations to particle and energy confinement time are caused by turbulence and collisions between particles, which determine the "anomalous" and the neoclassical transport levels respectively. In this work, we focus on the studies of the collision operator and applications to neoclassical physics, such as energy and particle transport, and the neoclassical bootstrap current. The neoclassical bootstrap current can drive instabilities in certain cases, hence it is important to understand when studying turbulence. To study these transport processes appropriate collision operators and kinetic simulations are needed. We give a brief review of the kinetic model and the collision operators, with a discussion on the simplifications and conservation properties. We implemented the simplified Lorentz collision operator in the TRIMEG code, a TRIangular MEsh-based Gyrokinetic code that can handle the open field line geometry. Using TRIMEG code and the newly implemented collision operator, we studied electron transport and bootstrap current generation with the consideration of density gradient but uniform temperature for different geometries. We compared the simulation results to theoretical calculations for simplified and realistic geometries. A good agreement between theory and our simulation results is observed for the large aspect ratio case in particle/energy fluxes and bootstrap current. Meanwhile, discrepancies are also observed for the moderate aspect ratio case and the ASDEX-Upgrade case, due to the different treatments and approximations in theory and simulation. The capability of the particle simulation in TRIMEG code has been demonstrated for the studies of electron transport and bootstrap current generation.

Chapter 1

Introduction

1.1 Motivation

The main motivation for the current work is fusion research. The aim of the field is to reach stable conditions for fusion processes to be possible and harness the resulting energy. For two protons to fuse it is required to overcome the Coulomb repulsion until the short-range nuclear forces take over. For this, they must have enough kinetic energy at which point they are in the plasma state. For a reactor to function, the thermonuclear power produced by the fusion reactions must be larger than the power loss. The condition when the fusion process is self-sustaining is called the ignition condition, and is a function of density, temperature, and the confinement time [33]. To satisfy these requirements a device called Tokamak has advanced the most as a plasma confinement device. It has a toroidal configuration that ensures that the magnetic field lines don't exit the volume, and hence there are no end losses. As particle trajectories to the lowest order follow the field lines, this should ensure good confinement of the plasma. However, after decades of research, scientists found numerous processes that deteriorate confinement [34]. Due to the toroidal shape of the device, there are transport processes that lead to the transport of the particles outside of the confinement device, this is called neoclassical transport. Furthermore, there are also transport processes that happen due to turbulence, called anomalous transport. The neoclassical transport in certain cases can be analytically calculated. In this work, we study the neoclassical physics of electrons by taking into account the collisional processes in toroidal geometry. In addition, we compare analytical solutions to our simulation results and benchmark the simulation code.

1.2 Plasma Physics

1.2.1 Plasma Properties

Plasma is an ionized gas, which has specific properties due to a large number of charged particles [33]. If we consider a small charge separation such as sheets of electron and ions in the plasma with length of l between them, and a density of n, the electromagnetic force per area will be $F \propto (lne)^2/\epsilon_0$. If we consider the approximate values for a Tokamak in $1cm^3$ lengths, $n \propto 10^{20}m^{-2}$ and $F \propto 10^9 Nm^{-2}$, which is a huge force. Hence, on macroscopic scales in the plasma

$$n_e = \sum_i n_i Z_i, \tag{1.1}$$

where, n_e, n_i are the electron and ion densities respectively, and Z_i is the ion charge number. This condition is called quasi-neutrality. However, if we move to small scales, at a specific length λ_D, called the Debye length and given by

$$\lambda_D = \sqrt{\frac{\epsilon_0 T}{ne^2}}, \tag{1.2}$$

charge separation can happen due to the thermal energy of the particles being the same scale as the electromagnetic force $F \propto nT$. This is also the scale to which a stationary ion's electric field in the plasma would extend, until being significantly shielded by the electron response. Furthermore, we approximate that the average potential energy is smaller than the kinetic energy, and we arrive to the condition that the number of particles in the Debye length should be sufficiently large, this quantity is also called the plasma parameter Λ and is given by [33]

$$\Lambda \equiv n\lambda_D^3 \gg 1. \tag{1.3}$$

If we consider the time scales on which the plasma reacts to charge density perturbations, we can write the equation of motion for particles in the electric field, and using the continuity equation arrive at the plasma oscillations. This describes the time scale of charge separation, also called the plasma frequency. The plasma frequency generally refers to the electron plasma frequency, as it is significantly larger for electrons than ions. It is given by

$$\omega_{p(q)} = \sqrt{\frac{nq^2}{\epsilon_0 m_q}}. \tag{1.4}$$

These oscillations are the fundamental timescale for plasma physics. For these to be visible in our system the oscillation frequencies of external effects need to be less than the plasma frequency. In addition, the following constraints are placed on these parameters:

$$\lambda_D \ll \text{Observation length scales} \quad \frac{2\pi}{\omega_p} \ll \text{Observation timescales.} \tag{1.5}$$

1.2.2   Particle Motion

We consider the motion of a charged particle in an electromagnetic field, with only magnetic and electric forces. The general equation of motion comes from the Lorentz force: [8]

$$m\vec{a} = q\left(\vec{E}(\vec{x},t) + \vec{v} \times \vec{B}(\vec{x},t)\right). \tag{1.6}$$

We start by only considering a static magnetic field $\vec{B} = B\hat{b} = B_0\hat{z}$, and no electric field. The force on the particle is perpendicular to the motion, hence the particle will move in a circle perpendicular to the field as shown in Figure 1.1, with the frequency

$$\Omega = \frac{qB_0}{m}, \tag{1.7}$$

also called the gyro-frequency, and the gyro-radius

$$\rho = \frac{mv_\perp}{qB_0}. \tag{1.8}$$

These quantities provide time scales and length scales, which describe magnetized plasma. While deriving the equations of motion, we will assume that our space and time scales are much larger than the gyro-radius and the gyro-frequency. In the cases of interest here, the plasmas are magnetized and it is useful to separate the gyration from the movement of the gyro-center:

$$\vec{x} = \vec{x}_{gc} + \frac{m\hat{b} \times \vec{v}}{qB} \tag{1.9}$$

where we define B in the position of the gyro-center. Now we can investigate the motion of the $\vec{x}_{gc}$. We can write the following:

$$\dot{\vec{x}}_{gc} = \vec{v}_{gc} = \vec{v} - \frac{m\hat{b}}{qB} \times \vec{a} \tag{1.10}$$

We can replace $\vec{a}$ using the Lorentz force, and assume that E is constant, we get the following result:

$$\vec{v}_{gc} = \vec{v}_\parallel + \frac{\vec{E} \times \vec{B}}{B^2} = \vec{v}_\parallel + \vec{v}_{E\times B}. \tag{1.11}$$

The term $\vec{v}_{E\times B}$ is called the E cross B drift, and it is also described in Figure 1.1. For an arbitrary force in the equation of motion, e.g. gravity $F = mg$, the additional drift term in the velocity of the gyro-center would be

$$\vec{v}_F = \frac{\vec{F} \times \vec{B}}{qB^2}. \tag{1.12}$$

Now if the magnetic field is static but not uniform, the radius is not constant during the gyration which causes changes to the overall guiding center drift.
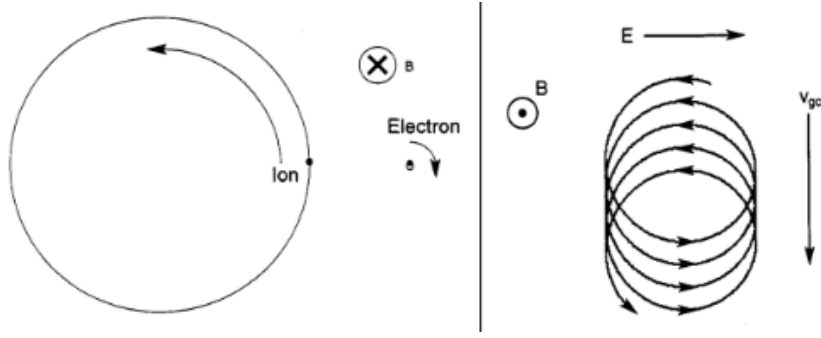
FIGURE 1.1: Motion of a particle in only static Magnetic field (left) and with additional Electric field (right). Taken from [8].

To describe this motion in a simple way, it is useful to expand the equation of motion to 1st order in $\epsilon = \rho/L$ and plug in the 0th order solution, where $L \equiv 1/|\nabla \ln B|$. The 0th order solution is

$$m\frac{dv_0}{dt} = q\vec{v}_0 \times \vec{B}_{gc}. \tag{1.13}$$

For the 1st order equation, we take into account the $\vec{B}$-field variation:

$$\vec{B} = B_{gc} - \frac{m}{qB_{gc}}\left(\left(\vec{v}_0 \times \hat{b}\right) \cdot \nabla\right)\vec{B}_{gc} \tag{1.14}$$

and time-average the equation of motion over many gyro periods. In addition, we have assumed there is no electric field and we finally arrive to the following drift equations (more detailed derivation in [8]):

$$\vec{v}_d = \frac{mv_\perp^2 \hat{b} \times \nabla B}{2qB^2} + \frac{mv_\parallel^2}{qB}\hat{b} \times (\hat{b} \cdot \nabla)\hat{b} \tag{1.15}$$

where the first term is called the gradient B drift $v_{\nabla B}$ and is caused by the gyro-radius being smaller in the high field region and is visualized in Figure 1.2. The second term is called the curvature drift $\vec{v}_c$, and this is caused by the curvature of the magnetic field, which imposes a centripetal acceleration and results in a drift perpendicular to the curvature and the initial velocity, as shown in Figure 1.2.

Now if we also consider that the electric field is varying in time but restrict our calculations to the case where the variation timescale is much larger than the gyro-period, we can calculate the additional drift term appearing in the gyro-center equation of motion, which is the second order in ϵ [8]:

$$v_p = \frac{m}{qB^2}\frac{d\vec{E}_\perp}{dt}, \tag{1.16}$$

which is also called polarization drift.

Finally, we consider the changes in particle motion due to a time-varying B field, which modifies the particle's parallel and perpendicular velocity in such a way that the adiabatic invariant - magnetic moment is conserved, as is described in detail in the following reference [8]. Here we restrict our discussion to slow time variations compared to the gyrofrequency. We observe that due to Faraday's law, a curl to the electric field is generated, which then accelerates the particle perpendicular to the magnetic field. In this case, it can be readily proven that a quantity μ is conserved given that the magnetic field is slowly varying. This quantity μ is called the magnetic moment defined as follows
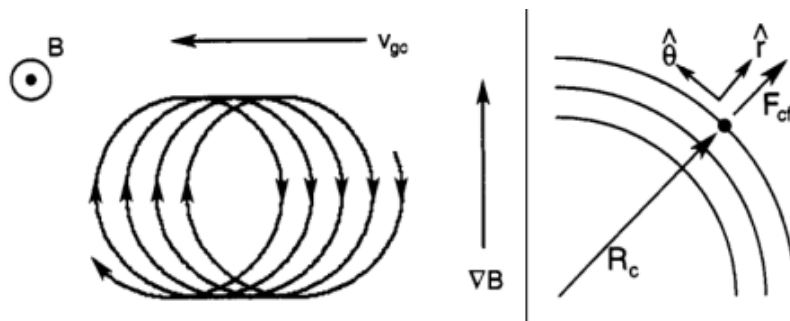
$$\mu = \frac{v_\perp^2}{2B}. \tag{1.17}$$

FIGURE 1.2: Drift due to the gradient of a magnetic field (left), and description of the curvature force on the particle due to curved magnetic field lines (right). Taken from [8].

1.3   Kinetic description

In general, when we study plasma physics, we have to consider the interaction of numerous particles. There are two frameworks used for this: the fluid model and the kinetic model. The fluid model describes the plasma in terms of low-order moments of the particle distribution function, this is appropriate when the response to perturbations is nearly identical for all particles at a given location, which is a valid assumption in certain cases. Thus, it describes the plasma using a few variables such as the density, the kinetic temperature, and the flow velocity. However, when the effects caused by the particle velocity differences are important, such as resonance caused by wave-particle interactions, it is important to use the kinetic model, which describes the plasma as a distribution function in the $(\vec{x}, \vec{v})$ space, the so-called phase space [10]. A "microscopic" distribution function $\mathcal{F}$ can be expressed as

$$\mathcal{F} = \sum_{i=1}^{N} \delta(\vec{x} - \vec{x}_i(t))\delta(\vec{v} - \vec{v}_i(t)). \tag{1.18}$$

The particle number density per infinitesimal volume around $\vec{x}$ is

$$n(\vec{x}, t) = \int d^3 v \mathcal{F}(\vec{x}, \vec{v}, t). \tag{1.19}$$

We can also write the charge density and current density using this formulation:

$$\rho = e \int d^3 v \mathcal{F}(\vec{x}, \vec{v}, t), \tag{1.20}$$

$$\vec{J} = e \int d^3 v \vec{v} \mathcal{F}(\vec{x}, \vec{v}, t). \tag{1.21}$$

The phase space volume is conserved as shown in Figure 1.3, which can also be interpreted as the particle number conservation. Therefore, we can write

$$\frac{\partial \mathcal{F}}{\partial t} + \vec{v} \cdot \nabla \mathcal{F} + \vec{a} \cdot \frac{\partial \mathcal{F}}{\partial \vec{v}} = 0, \tag{1.22}$$

where $\vec{a}$ satisfies

$$m\vec{a} = e(\vec{E} + \vec{v} \times \vec{B}). \tag{1.23}$$

This equation is exact, however, it involves delta functions and instantaneous
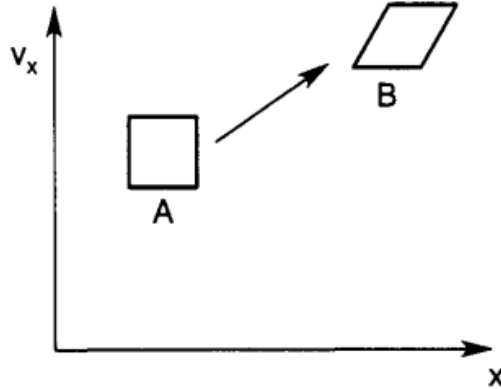
FIGURE 1.3: Evolution in time from A to B for 1-dimensional phase space distribution. Taken from [8].

changes, therefore solving it is as hard as solving a many-body problem. To simplify this problem, we consider an ensemble average of this distribution function which we call f and this is now a smooth function

$$f \equiv \bar{\mathcal{F}} = \langle \mathcal{F} \rangle_{ensemble}. \tag{1.24}$$

However, when writing the ensemble average of the acceleration, we have to consider that it depends on the trajectories of the particles, and it can not be simply written as

$$\langle \vec{a} \cdot \nabla \frac{\partial \mathcal{F}}{\partial \vec{v}} \rangle_{ensemble} \neq \bar{\vec{a}} \cdot \frac{\partial f}{\partial \vec{v}}. \tag{1.25}$$

The reason is that we have to consider the correlations between (numerous species of) particles, which is in general expressed by a complex function $C(f_{si})$. These correlations are mostly due to close encounters between them, hence $C(f_{si})$ is called the collision operator and can be expressed as follows

$$C(f_{si}) = \bar{\bar{a}} \cdot \frac{\partial f}{\partial \vec{v}} - \langle \vec{a} \cdot \frac{\partial \mathcal{F}}{\partial \vec{v}} \rangle_{ensemble}. \tag{1.26}$$

The kinetic theory analyzes this correlation with different approximations depending on the needs of the model at hand. Finally, the ensemble-averaged kinetic equation, also called the Vlasov-Maxwell equation is

$$\frac{\partial f}{\partial t} + \vec{v} \cdot \nabla f + \vec{a} \cdot \frac{\partial f}{\partial \vec{v}} = C(f_{si}), \tag{1.27}$$

where we have suppressed the bar over $\vec{a}$.

1.3.1   Collision operator

The collisional effects can be compared to the Brownian motion. Due to the sparse distribution of particles in space for most plasmas of our interest, we can assume that two-body collisions are dominant and are affected by the many-body physics such as Debye shielding, which make the effective interaction range finite [10]. Therefore, if we have multiple species of particles, the collision operator for species s can be written as the summation of the collision operators between all species of particles

$$C_s = \sum_{s'} C_{ss'}. \tag{1.28}$$

We will consider collision operators that guarantee particle, energy, and momentum conservation, which can be written as

$$\int d^3v C_{ss} = 0, \tag{1.29}$$

$$\int d^3v m_s \vec{v} C_{ss'} = -\int d^3v m_{s'} \vec{v} C_{s's}, \tag{1.30}$$

$$\int d^3v \frac{1}{2} m_s v^2 C_{ss'} = \int d^3v \frac{1}{2} m_{s'} v^2 C_{s's}. \tag{1.31}$$

When we consider the case with large plasma parameters $\Lambda \gg 1$, we can assume that each particle is affected simultaneously by the field of many surrounding particles. Due to the long range of shielded interaction, small-angle collisions will be dominant. Hence, we can treat the particle motion as a random walk where mild changes accumulate. This approximation is known as the Fokker-Planck approximation. We can now define a correlation time t_c, and after this, the behavior can be considered a random walk. Hence, if we

consider changes in time Δt much larger than the correlation time, we can define a probability $P(\vec{v}, \Delta \vec{v}, \Delta t)$ that particle with current velocity $\vec{v}$ will have a change of the magnitude $\Delta \vec{v}$. Then any distribution function can be written as

$$f(\vec{v}, t) = \int d^3 d\Delta v f(\vec{v} - \Delta \vec{v}, t - \Delta t) P(\vec{v} - \Delta \vec{v}, \Delta \vec{v}, \Delta t). \qquad (1.32)$$

As the probability quickly decreases for high values of $\Delta \vec{v}$, we can expand in powers of $|\Delta \vec{v}|$, and take averages $\langle ... \rangle$ relative to P and we get the general form of Fokker-Planck collision operator [10]

$$C(f) = -\frac{\partial}{\partial \vec{v}} \cdot (\frac{\langle \Delta \vec{v} \rangle}{\Delta t} f) + \frac{1}{2} \frac{\partial^2}{\partial \vec{v} \partial \vec{v}} : \left(\frac{\langle \Delta \vec{v} \Delta \vec{v} \rangle}{\Delta t} f \right). \qquad (1.33)$$

This can also be rewritten as

$$C(f) = -\frac{1}{m} \frac{\partial}{\partial \vec{v}} \cdot (\vec{R} f_s) + \frac{\partial}{\partial \vec{v}} \cdot \vec{D}(f) \cdot \frac{\partial f}{\partial \vec{v}}, \qquad (1.34)$$

with the second-rank diffusion tensor

$$\vec{D} = \frac{1}{2} \frac{\langle \Delta \vec{v} \Delta \vec{v} \rangle}{\Delta t}, \qquad (1.35)$$

and the velocity-dependent dynamical friction term

$$\vec{R} = m \frac{\langle \Delta \vec{v} \rangle}{\Delta t} + m \frac{\partial}{\partial \vec{v}} \cdot \vec{D}. \qquad (1.36)$$

Taking into account that this operator describes collisions between two species, this can also be rewritten as

$$C(f_{ss'}) = -\frac{1}{m_s} \frac{\partial}{\partial \vec{v}} \cdot (\vec{R}_{ss'}(f_{s'}) f_s) + \frac{\partial}{\partial \vec{v}} \cdot \vec{D}_{ss'}(f_{s'}) \cdot \frac{\partial f_s}{\partial \vec{v}}. \qquad (1.37)$$

Evaluation of $\vec{R}$ and $\vec{D}$ can be done using Newton's law in the screened potential field [27]. Using this we can write the diffusion tensor and the dynamical friction as integrals of the distribution function [10]

$$D_{ss'\alpha\beta} = \frac{\gamma_{ss'}}{m_s^2} \frac{\partial G_{s'}}{\partial v_\alpha \partial v_\beta}, \qquad (1.38)$$

$$R_{ss'\alpha} = \frac{2\gamma_{ss'}}{m_s^2} \frac{\partial H_{s'}}{\partial v_\alpha}, \qquad (1.39)$$

where G and H are called the Rosenbluth potentials and are given by

$$G_{s'}(\vec{v}) \equiv \int d^3 v' f_{s'}' |\vec{v} - \vec{v}'|, \qquad (1.40)$$

$$H_{s'}(\vec{v}) \equiv \int d^3 v' f_{s'}' |\vec{v} - \vec{v}'|^{-1}. \qquad (1.41)$$

The constant γ is

$$\gamma_{ss'} = \frac{e_{s'}^2 e_s^2 \log \Lambda_c}{8\pi\epsilon_0^2}, \tag{1.42}$$

where ϵ_0 is the electric constant, and $\log \Lambda_c$ is the Coulomb logarithm which is generally treated as a constant and depends on the ambient temperatures of the species [7]. This very general collision operator is an integral-differential function that is very complicated to solve and model, hence we use a simplified model from previous work [35, 21] by assuming a small deviation from the equilibrium Maxwellian distribution and linearizing the operator. This operator is

$$\begin{aligned}
C(\delta f_a) &= P(f_M, \delta f_b) + \frac{\partial}{\partial \mathbf{v}} \cdot (\mathbf{v} F \delta f_a) \\
&+ \frac{1}{2}\frac{\partial^2}{\partial \mathbf{v} \partial \mathbf{v}} : [G(\mathbf{I}v^2 - \mathbf{v}\mathbf{v}) + H\mathbf{v}\mathbf{v}]\delta f_a \ ,
\end{aligned} \tag{1.43}$$

with P corresponding to the energy and momentum conservation and F, G, and H functions defined as

$$F = \left(1 + \frac{m_a}{m_b}\right)\phi(x)\nu_0 \ , \tag{1.44}$$

$$G = \left[\left(1 - \frac{1}{2x}\right)\phi(x) + \frac{d\phi(x)}{dx}\right]\nu_0 \ , \tag{1.45}$$

$$H = \frac{1}{x}\phi(x)\nu_0 \ . \tag{1.46}$$

Here $x = v^2/v_{th,b}^2$ and $\phi(x)$ is the Maxwellian integral defined by

$$\phi(x) = \frac{2}{\sqrt{\pi}}\int_0^x e^{-t}\sqrt{t}\,dt \ , \tag{1.47}$$

and basic collision frequency ν_0 is

$$\nu_{0,\alpha\beta} = \frac{4\pi n_\beta e_\alpha^2 e_\beta^2 \log \Lambda_{\alpha\beta}}{m_\alpha^2 v^3}. \tag{1.48}$$

Additionally, when considering collisions between ions and electrons, the difference in mass between the species is large, and thus, we can neglect the mass of the electron to get the following collision operator, which is accurate to first order in $(1/x)$, consisting of pitch angle scattering and energy diffusion terms,

$$C_{ei}(\delta f_e) = \nu_0 \frac{1}{2}\frac{\partial}{\partial \xi}(1 - \xi^2)\frac{\partial}{\partial \xi} + \nu_0 v \frac{\partial}{\partial v}\left(\frac{m_e}{m_i}\delta f_e + \frac{v_{th,i}^2}{2v}\frac{\partial}{\partial v}\delta f_e\right) \ , \tag{1.49}$$

where $\xi = v_\parallel/v$ is called the pitch. If we treat the heavy species as infinitely massive, with negligible thermal velocity the collision operator becomes much simpler and we get the Lorentz collision operator [10]

$$C_{ei}(\delta f_e) = \nu_0 \frac{1}{2}\frac{\partial}{\partial \xi}(1 - \xi^2)\frac{\partial}{\partial \xi} \ . \tag{1.50}$$

Equation 1.50 is the collision operator we implemented in TRIMEG code for the neoclassical studies of electron transport and bootstrap current in this work.

1.3.2 Classical transport

We now discuss the diffusion of particles due to collisions in a straight magnetic field configuration. Then

$$\Gamma_r = -D\frac{\partial n}{\partial r}, \tag{1.51}$$

where Γ_r is the particle flux in the perpendicular direction to the magnetic field, and D is the diffusion coefficient. For two-particle collisions, considering the change in the gyro-center due to the collisions Δr_{gc}, and momentum conservation [30], we arrive at the following equation for each species j

$$\sum_j e_j \Delta r_j = 0. \tag{1.52}$$

This equation tells us that for like-species collisions, there is no net diffusion, and for inter-species collisions, the diffusion rate is the same for both ions and electrons. The estimate of the Diffusion coefficient for electrons by the random-walk argument is

$$D_{class} = \frac{(\Delta x)^2}{\Delta t}, \tag{1.53}$$

where Δx is the step length which we can assume to be equal to the gyro-radius ρ_e, and Δt is the time between collisions, which can be assumed to be proportional to the time between collisions of ions and electrons - $1/\nu_{ei}$. This heuristic estimation also agrees with more thorough derivations [30], and we can write the classical diffusion coefficient as

$$D_{class} \propto \rho_e^2 \nu_{ei}. \tag{1.54}$$

In the toroidal geometry of tokamak plasmas, the estimate of Δt and Δx is different, which leads to different diffusion coefficients, as we will discuss in the following chapter.

Chapter 2

Gyrokinetic model and particle simulations

2.1 Tokamak geometry and guiding center equations

A simple configuration for magnetic confinement, where the magnetic field lines form nested surfaces, is a torus. A tokamak is a toroidal chamber, where the primary field is the toroidal magnetic field, which is produced by poloidal currents in external coils. Additionally, there is a smaller poloidal magnetic field produced by the toroidal current in the plasma. Furthermore, there are also other, smaller contributions to the $\vec{B}$-fields due to coils used for plasma shaping, and poloidal currents in the plasma. The basic configuration is shown in Figure 2.1.
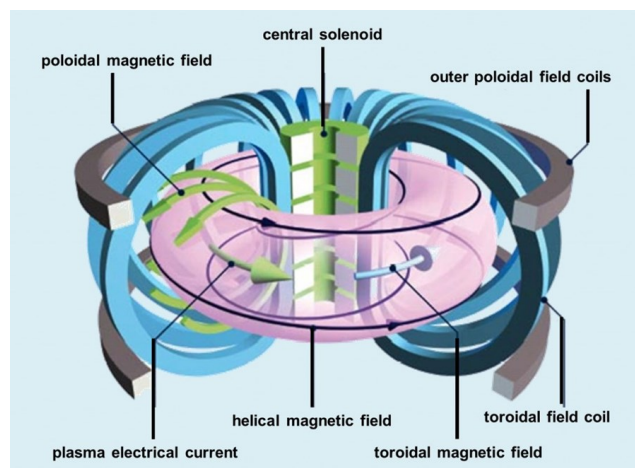

FIGURE 2.1: Magnetic fields and currents in a tokamak. Taken from [20].

2.1.1 Tokamak coordinates

When describing the tokamak, we assume that it is axisymmetric, and some of the coordinate systems we can use are either (R, Z, φ) or (r, θ, φ). They are shown in Figure 2.2.
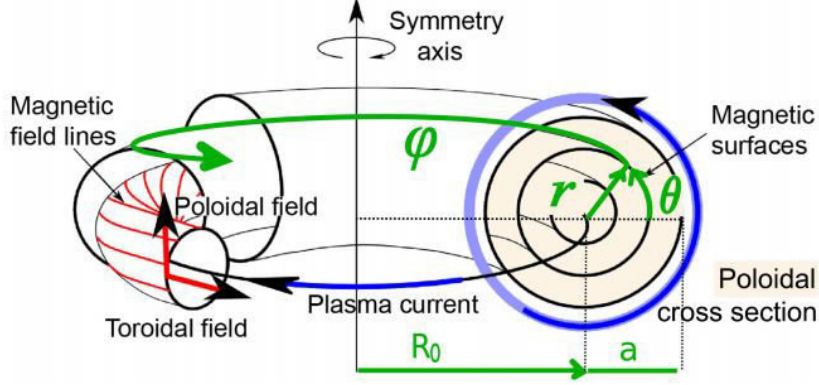

FIGURE 2.2: Tokamak (r, θ, φ) coordinates, where R_0 is called the major radius, and a is the minor radius. Taken from [6].

In the Cartesian coordinate system (X, Y, Z), the coordinates (R, Z, φ) are defined as follows,

$$R^2 = X^2 + Y^2, \tag{2.1}$$

$$\tan \varphi = Y/X, \tag{2.2}$$

$$Z = Z, \tag{2.3}$$

$$J_{(R,\varphi,Z)} = -R. \tag{2.4}$$

Here J represents the Jacobian. We can also write the following descriptions for the (r, θ, φ) coordinate system

$$R = R_0 + r \cos \theta, \tag{2.5}$$

$$Z = r \sin \theta, \tag{2.6}$$

$$J_{(r,\theta,\varphi)} = -rR. \tag{2.7}$$

In addition to these two coordinate systems, it is also helpful to describe the tokamak using the flux coordinates (ψ, θ, φ), shown in Figure 2.3. Here, the coordinate ψ is the magnetic field surface coordinate, and is linked to the magnetic field as follows,

$$\vec{B} \cdot \nabla \psi = 0, \tag{2.8}$$

$$B_R = -\frac{1}{R} \frac{\partial \psi}{\partial Z}, \tag{2.9}$$

$$B_Z = \frac{1}{R} \frac{\partial \psi}{\partial R}. \tag{2.10}$$

At the axis, $\psi = 0$ by definition and is increasing outward. For this coordinate system, the Jacobian is

$$J^{-1}_{\psi,\theta,\varphi} = \nabla\psi \cdot (\nabla\theta \times \nabla\varphi).$$ (2.11)

Additionally, when analyzing an arbitrary function F, we sometimes want to calculate the flux surface average of that function $\langle F \rangle$, which is defined as [12]

$$\langle F \rangle = \frac{d\psi}{dV} \int \frac{ds}{|\nabla\psi|} F.$$ (2.12)
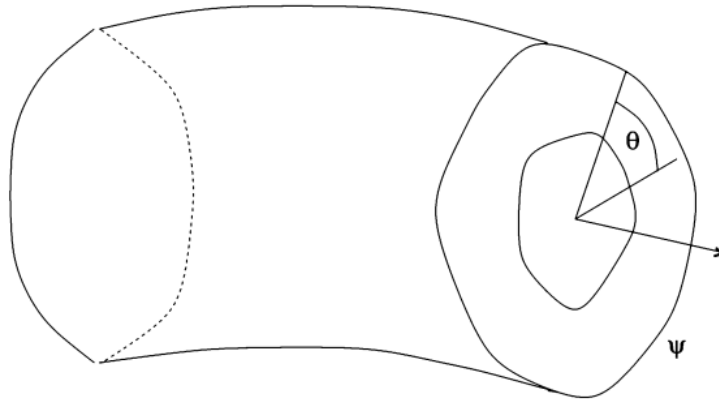
FIGURE 2.3: Tokamak flux coordinates. Taken from [34].

2.1.2 Equilibrium

To derive the equilibrium condition of the plasma, it is appropriate to use the Magnetohydrodynamic (MHD) description. This description treats the plasma as a hydrodynamic fluid that is affected by the electric and magnetic fields, with additional quasi neutrality and small Larmor radius approximations [8]. Assuming $n_e \approx n_i$, and the vacuum permeability $\mu_0 = 1$, the plasma

is described with the following equations:

$$\rho \approx nm_i, \tag{2.13}$$

$$\vec{u} \approx \vec{u}_i + \frac{m_e}{m_i}\vec{u}_e, \tag{2.14}$$

$$\vec{j} \approx n_e e(\vec{u}_i - \vec{u}_e), \tag{2.15}$$

$$\frac{\partial \rho}{\partial t} + \nabla(\rho\vec{u}) = 0, \tag{2.16}$$

$$\vec{E} + \vec{u} \times \vec{B} = \eta\vec{j}, \tag{2.17}$$

$$\rho\frac{\partial \vec{u}}{\partial t} = -\nabla p + \vec{j} \times \vec{B}, \tag{2.18}$$

$$\nabla \times \vec{B} = \vec{j}, \tag{2.19}$$

$$\nabla \times \vec{E} = -\frac{\partial \vec{B}}{\partial t}, \tag{2.20}$$

$$\nabla \cdot \vec{B} = 0. \tag{2.21}$$

Additionally, the pressure is assumed to be isotropic and defined as the sum of the momentum flux of both species. To have a complete set of equations, we also need to specify the time evolution of pressure, which can be defined as

$$\frac{d}{dt}\left(\frac{p}{\rho^{\gamma}}\right) = 0, \tag{2.22}$$

where γ is the heat capacity ratio from thermodynamics. From these equations, we see that the condition for a static equilibrium can be expressed as

$$\nabla p = \vec{j} \times \vec{B}. \tag{2.23}$$

In addition, from Equation 2.23, we can also obtain

$$\vec{B} \cdot \nabla p = \vec{j} \cdot \nabla p = 0, \tag{2.24}$$

which shows that magnetic field lines and current lie on surfaces of constant pressure-flux surfaces. A general representation of an axisymmetric magnetic field, which also satisfies $\nabla \cdot \vec{B} = 0$ is

$$\vec{B} = B_{\varphi} + B_{pol} = F(\psi)\nabla\varphi + \nabla\psi \times \nabla\varphi, \tag{2.25}$$

where $F(\psi)$ is the poloidal flux function [31]. If we plug this representation into the equilibrium Equation 2.23, and use Ampère's law, we arrive at the Grad-Shafranov equation:

$$R\frac{\partial}{\partial R}\left(\frac{1}{R}\frac{\partial \psi}{\partial R}\right) + \frac{\partial^2 \psi}{\partial Z^2} = -F(\psi)\frac{dF}{d\psi} - R^2\mu_0\frac{dp}{d\psi}. \tag{2.26}$$

For given $F(\psi)$ and $p(\psi)$ profiles this equation gives us the $\psi(R, Z)$ [31]. We can also define a new parameter $q(\psi)$, called the safety factor

$$q = \frac{\Delta\phi}{2\pi} = \frac{1}{2\pi}\oint\frac{1}{R}\frac{B_{\varphi}}{B_p}ds, \tag{2.27}$$

where $\Delta\phi$ is the increment of the toroidal angle following the magnetic field line corresponding to 2π increment in the poloidal direction, and s is the arc length in the poloidal direction. In general, the higher its value, the more stable is the configuration [33]. An approximation to the Grad-Shafranov equation is the ad hoc equilibrium, here we assume $\psi = \psi(r)$, $d\psi/dr = rB_0/\bar{q}(r)$, and $F = RB_\varphi = R_0B_0$. We assume axisymmetric magnetic surfaces, which are circular and concentric in poloidal cross-sections. The equation for the magnetic field now becomes

$$\vec{B} = \frac{B_0 R_0}{R}\left(\hat{e}_\varphi + \frac{r}{R_0\bar{q}(r)}\hat{e}_\theta\right),\qquad(2.28)$$

where vectors with a hat are the unit vectors. The $\bar{q}$ is called the pseudo-safety factor, which can be defined as a quadratic function

$$\bar{q} = \bar{q}_0 + (\bar{q}_{edge} - \bar{q}_0)\frac{r^2}{a^2},\qquad(2.29)$$

where a is the minor radius. It is related to q as

$$\bar{q}(r) = \sqrt{1 - \epsilon^2}q(r),\qquad(2.30)$$

where $\epsilon = r/R_0$ [31].

2.1.3   Guiding center equations

The guiding center equations of motion can be derived from the Lagrangian formalism [23] by starting with the Lagrangian for a charged particle in an electromagnetic field

$$L = [\vec{A}(\vec{v}, \vec{R}) + \vec{v}] \cdot \dot{\vec{R}} - H(\vec{v}, \vec{R}),\qquad(2.31)$$

where $\vec{B} = \nabla \times \vec{A}$ and $H = \vec{v}^2/2 + \Phi(\vec{R}, t)$. By separating the motion along the field line and the perpendicular motion, we can formulate the Lagrangian in terms of the guiding center coordinates. Furthermore, we assume that the Larmor radius and gyration period are much smaller than all the space and time variations in our system. Expanding in the small parameter of Larmor radius, and averaging over gyro-motion time scale, we arrive at the Lagrangian for the guiding center in second-order [34]

$$L = (\vec{A} + \frac{Ze\rho_\parallel \vec{B}}{m}) \cdot \vec{v} + \mu\dot{\xi} - H,\qquad(2.32)$$

where $\vec{v}$ is the guiding center velocity, $\rho_\parallel = mv_\parallel/(ZeB)$, μ is the magnetic moment redefined as $\mu = v_\perp{}^2/(2B)$, ξ is the gyro-phase and $\dot{\xi}$ is constant. If we insert the definition of the magnetic field in terms of flux functions given in Equation 2.25, we get the Lagrangian in our choice of coordinate system.

Using Lagrange's equations and our choice of coordinates, we find the guiding center equations in the axisymmetric configuration are [34, 24]

$$\dot{\vec{R}} = \frac{1}{Ze\vec{B} \cdot (\vec{B} + \rho_\parallel \nabla \times \vec{B})} \left(\frac{Z^2 e^2 B^2 \rho_\parallel}{m} \left(\vec{B} + \rho_\parallel \nabla \times \vec{B} \right) + \vec{B} \times \nabla H \right),$$

(2.33)

$$\dot{\rho}_\parallel = -\frac{1}{Ze\vec{B} \cdot (\vec{B} + \rho_\parallel \nabla \times \vec{B})} \left(\vec{B} + \rho_\parallel \nabla \times \vec{B} \right) \cdot \nabla H.$$

(2.34)

Equations 2.33–2.34 or their simplified/generalized forms have been implemented in various gyrokinetic codes such as , XGC [4], GTS [32], and TRIMEG [24, 25].

2.2 Neoclassical transport in tokamak plasmas

2.2.1 Basic features of the neoclassical transport

One key ingredient of neoclassical transport is geometry. Due to the shape of the torus, the ∇B and curvature drifts make the particles drift vertically upwards/downwards. In order to prevent the particles from escaping, the poloidal field is applied, which makes the particles move in circular orbits in the poloidal plane in addition to the toroidal motion. We can estimate the diffusion coefficient, by taking into account that during parallel motion particles have additional drift velocity contribution. Assuming that the average distance for particles traveling in the toroidal direction is Rq, and ν_{ei} is the collision frequency that electrons are scattered by ions, the neoclassical diffusion coefficient for electrons can be estimated as (the Pfirsch-Schlüter coefficient) [30]

$$D_{PS} \propto \nu_{ei} \rho_e^2 q^2.$$

(2.35)

In general, the average q is larger than 1, hence the neoclassical diffusion is larger than the classical diffusion for which $D_{cl} \propto \nu_{ei} \rho_e^2$. Note that in experiments the diffusion coefficients can be still much larger than the neoclassical diffusion, due to turbulence-induced anomalous transport [33]. The neoclassical transport is the minimum level of the net transport, if the turbulence can be mitigated. In this work, we focus on the neoclassical electron transport.

2.2.2 Particle orbits and banana, plateau, and collisional transport regimes

In the Tokamak due to the spatially changing magnetic field, the magnetic mirror effect confines the orbits of certain particles, given that

$$\left| \frac{v_\parallel}{v_\perp} \right| \leq \sqrt{2\epsilon},$$

(2.36)

where $\epsilon = r/R_0$ is the inverse aspect ratio. These particles are called trapped, and their orbits are shown in Figure 2.4. This can also be shown from the equation of motion considering how symmetries in $|\vec{B}|$ simplify particle orbits [34]. We can also estimate the frequency for these banana orbits called the
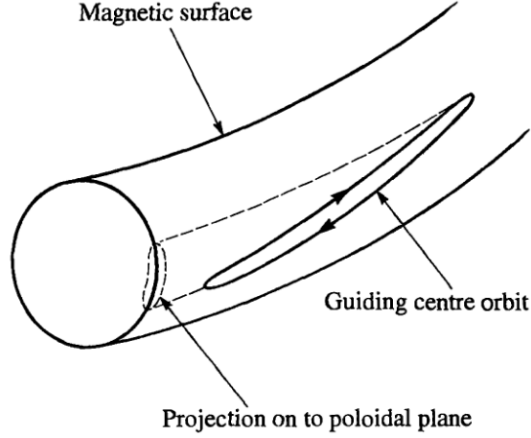

FIGURE 2.4: Banana orbits of trapped particles. Taken from [33].

bounce frequency [30]

$$\omega_B \propto \epsilon \frac{v_{th}}{qR}.\tag{2.37}$$

Furthermore, we can estimate the fraction of trapped particles by writing the condition for trapping. Assuming that the velocity distribution is isotropic, we find

$$\frac{\text{Trapped Particles}}{\text{Passing Particles}} = f_t \propto \sqrt{1 - \frac{B}{B_{max}}} = \sqrt{\epsilon(1 + \cos\theta)}.\tag{2.38}$$

If we integrate over a flux surface, we find that due to the dependence on ϵ, the number of trapped particles increases radially. Furthermore, due to the distribution of trapped particles in velocity space, the effective Lorentz collision frequency, which is just scattering through a velocity space pitch angle, is actually higher than for passing particles [30]

$$\nu_{eff,j} \propto \frac{\nu_j}{\epsilon}.\tag{2.39}$$

Now using the random walk argument we can estimate the trapped particle diffusion, which is actually different from the passing

$$D_{banana} = f_t \frac{(\Delta x)^2}{\Delta t} = \frac{\nu_{ei}\rho_i^2 q^2}{\epsilon^{3/2}}.\tag{2.40}$$

However, for this to be valid the trapped particles must be able to complete their orbits, therefore the effective collision frequency must be much smaller than the bounce frequency

$$\frac{\nu_{eff,e}}{\omega_B} = \nu^* = \frac{\nu_{ei}qR_0}{v_{th,e}\epsilon^{3/2}} \ll 1.\tag{2.41}$$

Furthermore, depending on the collision frequency there can actually be three regimes for the diffusion. If the collision frequency is high and the passing particles also collide before making poloidal orbits, this is called the Pfirsch-Schlüter or the collisional regime and the condition for this is

$$\nu^* \gg \epsilon^{-3/2}. \tag{2.42}$$

In the middle, we have the plateau regime, due to the fact that at the end of the banana regime and the beginning of the collisional regime, the diffusion coefficients coincide, as described in Figure 2.5.
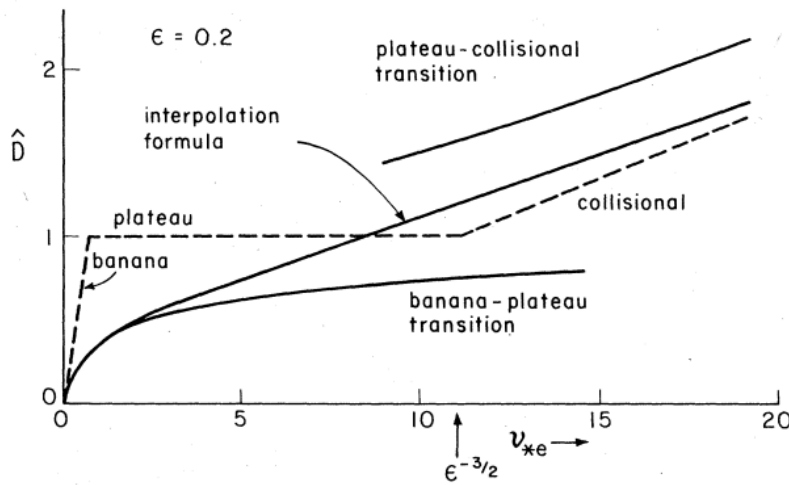

FIGURE 2.5: The different diffusion regimes, where the dashed line represents the asymptotic values for respective regimes. Taken from [12].

2.2.3 Bootstrap current

Due to collisional effects in banana orbits and the toroidal effect, a net toroidal current is produced. If we look at a single flux surface, in the presence of a finite radial density gradient, there is an asymmetry in density for particles co-moving with respect to the magnetic field and counter-moving, as shown in Figure 2.6. Therefore, due to collisions, there are passing particles migrating in velocity space and eventually forming the neoclassical equilibrium of the distribution function, featured by a shifted average parallel velocity. Thus, due to the density gradient in the radial direction, a net current can be produced in the toroidal direction. More generally, the temperature gradient can also generate the toroidal current, as we will discuss in Section 2.2.4. Considering two banana orbits, that have opposite velocities at $\theta = 0$, the density difference between the inner and outer banana orbits would be $\delta n = (dn/dr)W_b/2$, where W_b is the width of the banana orbit given by $W_b = \sqrt{R/r}q\rho$. Assuming that the average velocity of the trapped particles is $\rho/2$ and the pressure $p = n\rho^2/2$,

the formula for the bootstrap current can be written as

$$j_{bs} = -\sqrt{\frac{r}{R}} \frac{1}{B_\theta} \frac{\partial p}{\partial r}. \tag{2.43}$$

This current is sustained by radial outward flow of particles from more densely populated inner bananas to outer bananas [34]. This formula is independent of collisions and only assumes collisional relaxation of the particles for the current generation, however the number of trapped particles able to execute a full orbit also depends on the collision frequency, which will be taken into account in further discussions.
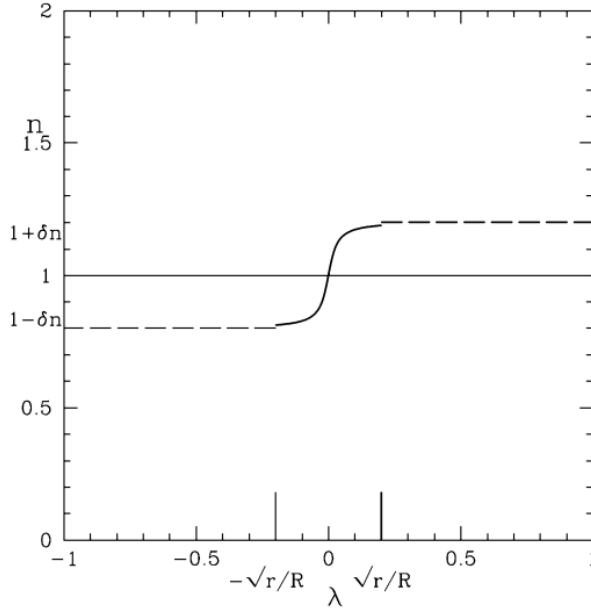

FIGURE 2.6: Particle density vs pitch defined here as $\lambda = v_\parallel/v$. The particles that have pitch within $-\sqrt{r/R} < \lambda < \sqrt{r/R}$ are trapped. $\delta n = (dn/dr)W_b/2$, where W_b is the width of the banana orbit. Taken from [34].

2.2.4   Kinetic theory of neoclassical transport

While the intuitive pictures of neoclassical transport and bootstrap current are given in Sections 2.2.1, 2.2.2 and 2.2.3, a comprehensive description has been summarized by making use of the kinetic theory [12, 2]. We can also derive a more thorough analysis of neoclassical transport starting from the drift-kinetic equation [12]

$$\frac{\partial f}{\partial t} + (\vec{v}_\parallel + \vec{v}_d) \cdot \nabla f + \frac{e}{m}\left[\frac{\partial \langle \Phi \rangle}{\partial t} + v_\parallel E_\parallel\right]\frac{\partial f}{\bar{\varepsilon}} = C(f, f), \tag{2.44}$$

where $\bar{\varepsilon} = \varepsilon + (e/m)(\langle \Phi \rangle - \Phi)$, $\varepsilon = mv^2/2$, and Φ is the electrostatic potential, while $\langle ... \rangle$ signifies flux surface average. The basis for simplification

is to expand this equation in powers of ρ_p, the poloidal gyro-radius. Further discussion closely follows the derivation from Hinton in 1976 [12]. After analyzing the ordering, expanding for each term in the equation, and assuming the Lorentz collision operator, the following equations are obtained to the first order for electrons and ions respectively

$$\vec{v}_\parallel \cdot \nabla f_{e1} - C_e f_{e1} = Iv_\parallel \cdot \nabla(v_\parallel/|\Omega_e|)\frac{\partial f_{e0}}{\partial \psi} - (e/T_e)v_\parallel E_\parallel f_{e0}, \quad (2.45)$$

$$\vec{v}_\parallel \cdot \nabla f_{i1} - C_{ii} f_{i1} = -I\vec{v}_\parallel \cdot \nabla(v_\parallel/|\Omega_i|)\frac{\partial f_{i0}}{\partial \psi}$$

$$+ v_\parallel(n_{i0}Z_i e E_\parallel + F_{\parallel i})\frac{f_{i0}}{p_{i0}}, \quad (2.46)$$

where f_0 is the zeroth order solution assumed to be Maxwellian, $I \equiv |J_{\psi,\theta,\varphi}|\nabla\psi\times\nabla\theta\cdot\vec{B}$, $F_\parallel$ is the parallel friction force, and Ω is the gyro-frequency. Furthermore, $C_e \equiv C_{ee} + C_{ei}$, and all the collision operators are linearized assuming that the distribution functions are nearly Maxwellian and gyro-phase-averaged. To simplify these equations, the functions H_e and H_i are introduced as follows

$$f_{e1} = \frac{2v_\parallel u_{i\parallel}}{v_{th,e}^2}f_{e0} - (e/T_e)f_{e0}\int_0^{l_p}\frac{dl_p}{B_p}[BE_\parallel - B^2\langle E_\parallel B\rangle/\langle B^2\rangle]$$

$$+ v_\parallel f_{se}B\langle E_\parallel B\rangle/\langle B^2\rangle + H_e \quad (2.47)$$

$$f_{i1} = -\frac{v_\parallel h}{\Omega_{ip}}\left[\frac{\partial \ln p_i}{\partial \rho} + \frac{Z_i e}{T_i}\frac{\partial \langle \Phi\rangle}{\partial \rho}\right]f_{i0}$$

$$+ (Z_i e/T_i)f_{i0}\int_0^{l_p}\frac{dl_p}{B_p}[BE_* - B^2\langle E_* B\rangle/\langle B^2\rangle] + H_i, \quad (2.48)$$

with $E_* \equiv E_\parallel - F_{\parallel i}/n_{i0}Z_i e$, and the integration path l_p is tangent to poloidal projection of the field line on a plane of constant φ. Using this definition we can write the equations that H_e and H_i satisfy and simplify them by splitting H_e and H_i into four and two parts, respectively, as functions of g_n

$$H_e = \sum_{n=1}^4 g_{ne}A_{ne}, \quad H_i = \sum_{n=1}^2 g_{ni}A_{ni}. \quad (2.49)$$

Hence, the transport problem is now reduced to calculating g_{ne} and g_{ni}. Therefore, we're left with the form

$$\vec{v}_\parallel \cdot \nabla H_e - C_e H_e = -\sum_{n=1}^4 \alpha_n A_{ne}f_{e0} \quad (2.50)$$

$$\vec{v}_\parallel \cdot \nabla H_i - C_{ii} H_i = -\sum_{n=1}^4 \beta_n A_{ni}f_{i0} \quad (2.51)$$

where A_{ni} and A_{ne} are general forces arising from the effective electric field, the density and temperature gradients, while α_n and β_n are functions of velocities

and geometry/equilibrium variables. The exact definitions for the coefficients can be found in equations (5.53)-(5.59) in the reference [12].

The analytical expressions can be obtained using the solutions H_i and H_e for the electron flux Γ_e, the electron and ion heat flux q_e, q_i, and average parallel current density $J_\parallel$ which are defined as

$$\Gamma_e \equiv \left\langle \int d^3 v \vec{v}_{de} \cdot \nabla \rho H_e \right\rangle = \left\langle \int d^3 \alpha_1 H_e \right\rangle, \qquad (2.52)$$

$$q_e/T_e \equiv \left\langle \int d^3 v \vec{v}_{de} \cdot \nabla \rho (v^2/v_{the}^2 - 5/2) H_e \right\rangle = \left\langle \int d^3 v \alpha_2 H_e \right\rangle, \qquad (2.53)$$

$$q_i/T_i \equiv \left\langle \int d^3 v \vec{v}_{di} \cdot \nabla \rho (v^2/v_{thi}^2 - 5/2) H_i \right\rangle = \left\langle \int d^3 v \beta_2 H_i \right\rangle, \qquad (2.54)$$

$$\frac{1}{T_e} \left\langle (J_\parallel - J_{\parallel s})/h \right\rangle \equiv \left\langle \int d^3 v \alpha_3 H_e \right\rangle, \qquad (2.55)$$

where $J_{\parallel s} \equiv \sigma_\parallel B \left\langle E_\parallel B \right\rangle / \left\langle B^2 \right\rangle$ is the Spitzer current density. The Equations 2.52-2.55 can be rewritten as

$$\Gamma_e = \sum_{n=1}^{4} (\alpha_1, g_{ne}) A_{ne}, \qquad (2.56)$$

$$q_e/T_e = \sum_{n=1}^{4} (\alpha_2, g_{ne}) A_{ne}, \qquad (2.57)$$

$$q_i/T_i = \sum_{n=1}^{2} (\beta_2, g_{ni}) A_{ni}, \qquad (2.58)$$

$$\frac{1}{T_e} \left\langle (J_\parallel - J_{\parallel s})/h \right\rangle = \sum_{n=1}^{4} (\alpha_3, g_{ne}) A_{ne}, \qquad (2.59)$$

where terms (β_n, g_{2n}) are the inner products defined as

$$(\beta_n, g_{mi}) \equiv \left\langle \int dv^3 \beta_n g_{mi} \right\rangle. \qquad (2.60)$$

Finally, the analytical solutions can be written using dimensionless electron transport coefficients K_{mn} which are related to the inner products and a detailed definition can be found in equations [6.114-6.119] in [12], and assuming

weak-coupling between electrons and ions:

$$\Gamma_e = -n_e\epsilon^{1/2}(\rho_\theta^2/\tau_e)\left(K_{11}A'_{1e} + K_{12}\frac{\partial}{\partial r}\ln T_e\right) \quad (2.61)$$

$$-K_{13}n_e\epsilon^{1/2}c\left\langle E_\parallel/h\right\rangle/B_{po}, \quad (2.62)$$

$$q_e + \frac{5}{2}T_e\Gamma_e = -n_eT_e\epsilon^{1/2}(\rho_{e\theta}^2/\tau_e)\left(K_{12}A'_{1e} + K_{22}\frac{\partial}{\partial r}\ln T_e\right) \quad (2.63)$$

$$-K_{23}n_eT_e\epsilon^{1/2}c\left\langle E_\parallel/h\right\rangle/B_{po}, \quad (2.64)$$

$$\left\langle (J_\parallel - J_{\parallel s})/h\right\rangle = -n_eT_e\epsilon^{1/2}(c/B_{po})\left(K_{13}A'_{1e} + K_{23}\frac{\partial}{\partial r}\ln T_e\right) \quad (2.65)$$

$$-K_{33}\epsilon^{1/2}\sigma_\parallel\left\langle E_\parallel/h\right\rangle, \quad (2.66)$$

where $\epsilon = r/R_0$, $\rho_{e\theta}^2 = 2m_eT_ec^2/e^2B_{po}^2$, $1/\tau_e = 4\nu_{ei}/(3\sqrt{\pi})(v/v_{th})^3$ and A'_{1e} is a combined force defined as

$$A'_{1e} = \frac{\partial}{\partial r}\ln p_e - \frac{5}{2}\frac{\partial\ln T_e}{\partial r} + \frac{T_i}{Z_iT_e}\left(\frac{\partial}{\partial r}\ln p_i - \frac{(\beta_1, g_{2i})}{1+\nu_{*e}^2\epsilon^2}\frac{\partial\ln T_i}{\partial r}\right). \quad (2.67)$$

In the above definition, ν_{*e} is similar to Equation 2.41, with an additional factor $\nu_{*e} = 4\nu^*/(3\sqrt{\pi})$. Furthermore, the following approximations were made in all collisionality regimes $(\alpha_3, g_{4e})/(\alpha_3, g_{1e}) \sim 1$ and for $n = 1$ or 2

$$(\alpha_n, g_{4e}) \simeq (\alpha_n, g_{1e}) \quad \text{(Banana-plateau)}, \quad (2.68)$$
$$(\alpha_n, g_{4e}) \simeq (\alpha_n, g_{1e})/(1+\nu_{*e}^2\epsilon^2) \quad \text{(Plateau-collisional)},$$
$$(\alpha_n, g_{4e})/(\alpha_n, g_{4e}) \sim \nu_{*e}^{-2}\epsilon^{-2} \ll 1 \quad \text{(Collisional)}.$$

The analytical expressions for which the coefficients were fitted are for $m, n = 1$ or 2

$$K_{mn} = K_{mn}^{(0)}\left(\frac{1}{1+a_{mn}\nu_{*e}^{1/2}+b_{mn}\nu_{*e}} + \frac{\epsilon^{3/2}(c_{mn}^2/b_{mn})\nu_{*e}\epsilon^{3/2}}{1+c_{mn}\nu_{*e}\epsilon^{3/2}}\right), \quad (2.69)$$

and for $n = 3$

$$K_{m3} = K_{m3}^{(0)}[1+a_{m3}\nu_{*e}^{1/2}+b_{m3}\nu_{*e}]^{-1}[1+c_{m3}\nu_{*e}\epsilon^{3/2}]^{-1}. \quad (2.70)$$

The values for numerical coefficients $K_{mn}^{(0)}, a_{mn}, b_{mn}$ and c_{mn}, where obtained for the cases in the banana-plateau regime

$$K_{mn} \simeq K_{mn}^{(0)}[1+a_{mn}\nu_{*e}^{1/2}+b_{mn}\nu_{*e}]^{-1}, \quad (2.71)$$

and the plateau-collisional regime

$$K_{mn} \simeq \epsilon^{3/2}(c_{mn}/b_{mn})K_{mn}^{(0)}\left(1 + \frac{1}{c_{mn}\nu_{*e}\epsilon^{3/2}(1+c_{mn}\nu_{*e}\epsilon^{3/2})}\right)$$
$$\text{(for n=1 or 2)}, \quad (2.72)$$

$$K_{m3} \simeq (K_{m3}^{(0)}/b_{mn}\nu_{*e})[1+c_{mn}\nu_{*e}\epsilon^{3/2}]^{-1}$$
$$\text{(for n=3)}. \quad (2.73)$$

For $\epsilon \ll 1$, values for the numerical coefficients can be found in Table 3 in [12]. These expressions will be used in chapters 4.1-4.5 to compare the simulation results to the analytical theory.

2.3   Numerical methods in particle simulations

In this section, numerical methods in particle simulations are discussed from a general point of view. These schemes are closely related to our current studies of electron transport in TRIMEG code as we will discuss in Chapter 3.

2.3.1   Discretization of the distribution function

When representing the distribution function in simulations, we need to discretize it. The total number of physical particles in the system is [16]

$$N_{ph} = \int f(z)J(z)dz, \tag{2.74}$$

where $z = (\vec{x}, \vec{v})$ represents a generalized phase-space coordinate, and $J(z)$ is the Jacobian. The number of physical particles in our system can be orders of magnitude larger than what can be stored in computer memory, hence markers are used, each of which represents more than just a single physical particle. The marker distribution function is

$$g(z) \approx \sum_{i=1}^{N} \frac{\delta(z - z_i(t))}{J(z)}, \tag{2.75}$$

where N is the number of markers that are used in the simulation. Furthermore, the following condition is assumed to be satisfied by the marker distribution function

$$\frac{dg(z,t)}{dt} = 0, \tag{2.76}$$

where d/dt specifies the collisionless case such as

$$\frac{d}{dt} = \frac{\partial}{\partial t} + \vec{v} \cdot \nabla + \vec{a} \cdot \nabla_{\vec{v}}. \tag{2.77}$$

With these definitions, the particle distribution function can be written as [25, 9]

$$f(z,t) = \frac{N_{ph}}{N} P_{tot}(z,t) g(z,t) \approx \frac{N_{ph}}{N} \sum_{i=1}^{N} p_{i,tot} \frac{\delta(z - z_i(t))}{J(z)}, \tag{2.78}$$

where $p_{i,tot} = P(z_i(t), t)$ is the weight field. This definition gives the full-f discretization. To further reduce the simulation time by simulating fewer markers while maintaining a sufficient signal-to-noise ratio, the distribution function can be split into two parts $f = f_0 + \delta f$. Here f_0 represents the background distribution function, and δf represents the perturbation. They can be represented as follows with respective weight fields analogously to Equation

2.78:

$$f_0(z,t) = \frac{N_{ph}}{N} P(z,t) g(z,t) \approx \frac{N_{ph}}{N} \sum_{i=1}^{N} p_i \frac{\delta(z - z_i(t))}{J(z)}, \tag{2.79}$$

$$\delta f(z,t) = \frac{N_{ph}}{N} W(z,t) g(z,t) \approx \frac{N_{ph}}{N} \sum_{i=1}^{N} w_i \frac{\delta(z - z_i(t))}{J(z)}. \tag{2.80}$$

Furthermore, the time evolution for the weights in the collisionless case can be written as

$$\frac{d}{dt} w_i(t) = -p_i \frac{d}{dt} ln f_0(z_i(t)), \tag{2.81}$$

$$\frac{d}{dt} p_i(t) = p_i \frac{d}{dt} ln f_0(z_i(t)), \tag{2.82}$$

$$\frac{d}{dt} (w_i(t) + p_i(t)) = 0. \tag{2.83}$$

Assuming that the background distribution is of zeroth order in ρ_p/R_0, where ρ_p is the poloidal gyro-radius, the time evolution for the weight equation can be written as [21]

$$\frac{dw}{dt} = (1 - w)\vec{v}_d \cdot (-\frac{d \ln f_0}{d\vec{x}}). \tag{2.84}$$

To take into account the collision effects, at each time step the collision operators can be applied after the collisionless dynamics [16]. Theoretically, the collision operator is taken into account in particle simulations by solving the Langevin equation, as we will discuss in the following section.

2.3.2 Numerical treatment of the collision operator in particle simulations

Treating the Fokker-Planck equation given in Equation 1.33 numerically, which is a partial differential equation (PDE), can be simplified using the Langevin approach [5]. Ito and Stratonovich algebras allow to link the PDE to a Langevin equation which is a stochastic differential equation (SDE). SDEs are easier to handle in simulation codes [5]. Hence, the Fokker-Planck equation can be rewritten as

$$\frac{\partial F}{\partial t} = -\frac{\partial}{\partial \vec{v}} \cdot \left[\Gamma_{ab} F_a - \frac{\partial}{\partial \vec{v}} \cdot (D_{ab} F_a) \right], \tag{2.85}$$

which is equivalent to the stochastic differential equation for each particle or marker,

$$\frac{d\vec{v}}{dt} = \Gamma_{ab} + G_{ab} d\vec{W}, \tag{2.86}$$

where $G_{ab} \cdot G_{ab}^T = 2D_{ab}$ and $\vec{W}$ stand for a Wiener process. This can be discretized using the Euler-Maruyama scheme [5]

$$\Delta \vec{v}^{ab} = \Gamma_{ab} \Delta t + G_{ab} \sqrt{\Delta t} \vec{R}^b, \tag{2.87}$$

where R_b is a vector of three independent random numbers. However, without any approximation, the potentials defined in Equations 1.40-1.41 have to be computed for each Langevin kick, which would result in $O(N^2)$ computation complexity for the number of markers. By making analytical approximations for the potentials and distribution function and using expansions and truncation, a complexity of $O(N)$ can be achieved. The Rosenbluth potentials can be expressed using expansion of the distribution function around an unshifted Maxwellian. Afterward, the truncation is made for high-order moments. The sensitivity for numerical resolution is high for higher-order moments, and they are also more effectively damped due to collisions hence the truncation is justified. However, the truncation now removes momentum and energy conservation, which would be removed regardless due to numerical resolution. This raises the issue of a correction term to be added to the collision operator C_{ab}^{corr}. The full non-linear collision operator can be written as

$$
\begin{aligned}
C_{ab}(f_a, f_b) &= C_{ab}(f_{Ma}, f_{Mb}) + C_{ab}(\delta f_a, f_{Mb}) \\
&+ C_{ab}(f_{Ma}, \delta f_b) + C_{ab}(\delta f_a, \delta f_b),
\end{aligned} \tag{2.88}
$$

where the linear operator can be obtained if the last term is removed. In addition, the field part $C_{ab}(f_{Ma}, \delta f_b)$ is also difficult to handle and is approximated. The method proposed by Lin [21] is to use the collision operator properties. Using the linearized collision operator given in Equation 1.43 and averaging over the gyro-phase gives the following equation

$$
\begin{aligned}
C(\delta f) =& \frac{\partial}{\partial v_\parallel}(\nu_{s\parallel}\delta f) + \frac{\partial}{\partial v_\perp^2}(\nu_{s\perp}\delta f) + \frac{\partial^2}{\partial v_\parallel \partial v_\perp^2}(\nu_{\parallel\perp}\delta f) \\
&+ \frac{1}{2}\frac{\partial^2}{\partial v_\parallel^2}(\nu_\parallel \delta f) + \frac{1}{2}\frac{\partial^2}{(\partial v_\perp^2)^2}(\nu_\perp \delta f) + P,
\end{aligned} \tag{2.89}
$$

with δf representing the gyro-center distribution, where collision coefficients $\nu_{s\parallel}, \nu_{s\perp}, \nu_\perp, \nu_\parallel, \nu_{\perp\parallel}$ are functions of F, G and H given in Equations 1.44-1.46, the exact definition of these coefficients can be found in the reference [21]. The test particle drag and diffusion terms can be implemented using the following Monte-Carlo method [35]

$$
v_\parallel = v_{\parallel 0} - \nu_{s\parallel}\Delta t + \sqrt{12}(R_1 - 0.5)\sqrt{\nu_\parallel \Delta t}, \tag{2.90}
$$

$$
\begin{aligned}
v_\perp^2 =& v_{\perp 0}^2 - \nu_{s\perp}\Delta t + \sqrt{12}(R_2 - 0.5)\sqrt{\left(v_\perp - \frac{v_{\parallel\perp}^2}{\nu_\parallel}\right)\Delta t} \\
&+ \sqrt{12}(R_1 - 0.5)\frac{\nu_{\parallel\perp}}{\nu_\parallel}\sqrt{\nu_\parallel \Delta t}.
\end{aligned} \tag{2.91}
$$

The momentum and energy conservation term P can be calculated analytically, and this term can be implemented by changing particle weights. This ensures the conservation of first-order momentum and energy and is given by [35]

$$
\Delta w = -\vec{v} \cdot \partial \vec{P} - \left(\frac{v^2}{v_{th,\alpha}^2} - \frac{3}{2}\right)\delta E \tag{2.92}
$$

where $\delta\vec{P}$ and δE are given by

$$\delta\vec{P} = \frac{2}{nv_{th\alpha}^2} \sum_i w_i \Delta\vec{v}_i, \tag{2.93}$$

$$\delta E = \frac{2}{3nv_{th\alpha}^2} \sum_i w_i \Delta v_i^2. \tag{2.94}$$

As shown by Lin [21] this method does not take into account the velocity dependence of the energy and momentum loss rates, which if taken into account shows better agreement in preserving the shape of a shifted Maxwellian in velocity space, and gives correct energy fluxes unlike the formulation in Equation 2.92. After taking into account the velocity dependence, the change in weight is represented by

$$\Delta w = -3\sqrt{\frac{\pi}{2}}\phi(x)\left(\frac{v_{th\alpha}}{v}\right)^3 \vec{v} \cdot \delta\vec{P} - 3\sqrt{\frac{\pi}{2}} \times \left(\phi(x) - \frac{d\phi(x)}{dx}\right)\frac{v_{th\alpha}}{v}\delta E, \tag{2.95}$$

where ϕ is given in Equation 1.47. In this work only the electron-ion Lorentz collision operator is used, given by Equation 1.50, which is written using the Monte-Carlo method as [21]

$$\xi = \xi_0(1 - \nu\Delta t) + (R - 0.5)[12(1 - \xi_0^2)\nu\Delta t]^{1/2}, \tag{2.96}$$

where $\xi = v_\parallel/v$, and R is a uniform random number between 0 and 1 [21]. Hence, in our simulation we have implemented the discretized version of the collision equation described by equation 1.50, as shown in equation 2.96.

2.3.3 Solving Equations Numerically

The equations of the kinetic system are the Boltzmann equation and the Poisson equation for the electric potential that yields the electric field. One of the popular methods for tackling this problem is the particle-in-cell (PIC) method. The algorithm is to randomly or pseudo-randomly initialize the particles and then solve the equations of motion to model their evolution. The time scheme for the equation of motion in the simplest case can be the Euler scheme. In this scheme, we deal with the initial value problem, where the time derivative $F' = \mathcal{F}(t, F)$ is known, and the initial value of the function at $t = 0$ is also known. Given a time step size Δt such as for any function F

$$F_{t+1} = F_t + \Delta t F_t'. \tag{2.97}$$

This scheme gets closer to the real solution for smaller step sizes. A similar method that provides better convergence for the same time step size is the Runge-Kutta method (sometimes also called RK4), where the evolution is calculated as

$$F_{t+1} = F_t + \frac{1}{6}\Delta t(k_1 + 2k_2 + 2k_3 + k_4), \tag{2.98}$$

and the k coefficients are

$$k_1 = \mathcal{F}(t, F_t), \tag{2.99}$$

$$k_2 = \mathcal{F}(t + \frac{\Delta t}{2}, F_t + \Delta t \frac{k_1}{2}), \tag{2.100}$$

$$k_3 = \mathcal{F}(t + \frac{\Delta t}{2}, F_t + \Delta t \frac{k_2}{2}), \tag{2.101}$$

$$k_4 = \mathcal{F}(t_n + \Delta t, F_t + \Delta t k_3). \tag{2.102}$$

For the equations of motion, the electric field values are needed. The electric field is calculated on a grid. There are a number of grid-based methods to solve the Poisson equation such as the finite difference method, the Fourier spectral method, and the finite element method [29]. In TRIMEG, JOREK, ORB5 and GYGLES, the finite element method is used. For solving the field equations, we look for the solution in a finite-dimensional vector space with a set of basis functions, and the solution is determined by the coefficients of the given basis. Hence, in a general case given the Equation [14]

$$\mathcal{L}\Phi = f, \tag{2.103}$$

where $\mathcal{L}$ is a linear differential operator, $f(x)$ is a known function, and $\Phi(x)$ is the function to be solved. Each of these functions can be represented in the chosen basis as

$$\Phi = \sum_{i=1}^{N} \phi_i \varphi_i(x), \quad f = \sum_{i=1}^{N} f_i \varphi_i(x), \tag{2.104}$$

where φ_i are the basis functions. A choice for the basis functions could be the B-spline functions which are continuous piece-wise cubic functions that have up to continuous second derivatives, as shown in Figure 2.7.

Introducing a test function $V(x)$ into the differential equation as

$$\int_a^b L(U)V dx = \int_a^b fV dx, \tag{2.105}$$

where integral is over the domain $a \leq x \leq b$. Requiring that this equation be satisfied for every test function gives us the weak form of the original differential equation, and this form can be discretized using the Galerkin method [14]. If we plug Equations 2.104 in the weak form and assume that the linear operator is $\mathcal{L} = -p\frac{d^2}{dx^2}$, after integrating by parts we get the following equation

$$\sum_{j=1}^{N} p \left(\int_a^b \varphi'_k \varphi'_j dx \right) \phi_j = \int_a^b f\varphi_k dx \tag{2.106}$$

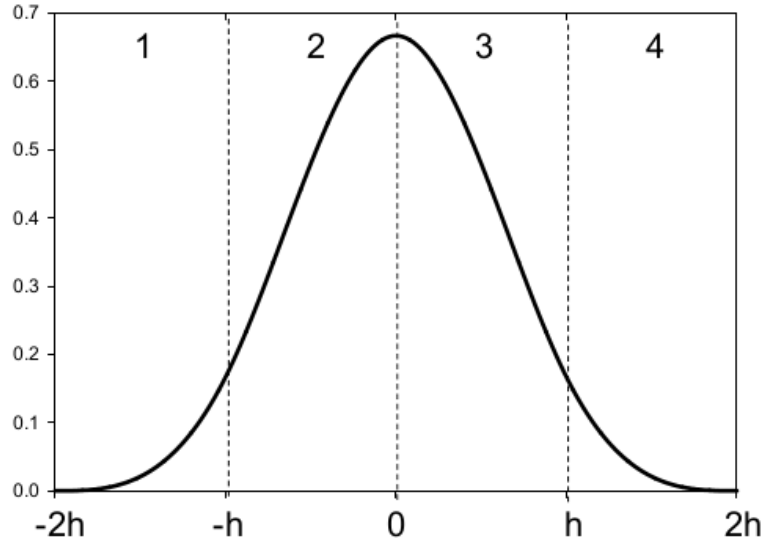where k is the degrees of freedom of the solution space S. This equation can

FIGURE 2.7: Basic cubic B-spline basis function. Taken from [14].

be also expressed as a matrix equation

$$M_{L,kj}\phi_j = M_{R,kj}f_k, \tag{2.107}$$

$$M_{L,kj} = \int_a^b p\phi'_k\phi'_j dx \ , \tag{2.108}$$

$$M_{R,kj} = \int_a^b \phi_k\phi_j dx \ , \tag{2.109}$$

which can be solved efficiently as described in more detail in [14]. For treating the realistic geometry of tokamak plasmas, the two-dimensional or three-dimensional finite element solvers are developed in various codes with details given in previous literature [19, 13, 9, 16, 24].

Chapter 3

Physics model and equations

3.1 TRIMEG (TRIangular MEsh based Gyrokinetic code)

3.1.1 General description of TRIMEG code

The main code used for the studies of neoclassical physics and the development of the physics module in this work is the TRIangular MEsh based Gyrokinetic (TRIMEG) code [24]. In the TRIMEG code, an unstructured mesh-based finite element method is adopted in the poloidal cross-section, and a Fourier decomposition scheme is adopted in the toroidal direction, which is a mixed Particle in cell - Particle in Fourier (PIC-PIF) scheme. While the calculations in the poloidal cross-section use the Finite element method described in section 2.3.3, the calculations in the toroidal direction are made using the PIF method described in [24]. However, in this work, axisymmetry in the toroidal direction ($n = 0$) is adopted for the study of neoclassical physics, without addressing instabilities or turbulence. TRIMEG has the possibility of also including the open field line region (OFL), which allows the simulation of the full plasma volume.

The poloidal cross-section is divided into triangles as shown in Figure 3.1. Based on the particle's position with respect to the triangles, the space characteristics such as field or density are calculated by using the finite element method and the Fourier decomposition, while also taking into account the proximity of the marker to the triangle's vertices and calculating the contribution proportionally. The mesh can be arbitrarily dense, which improves the accuracy of the space characteristics [24]. The code is divided into three physics classes: particles, field, and equilibrium. The normalization used is described in Table 3.1. The equilibrium information is loaded using the EQDSK file from Equilibrium reconstruction codes [17] and the magnetic field can be represented as Equation 2.25, and using B-spline subroutines the B-field com-
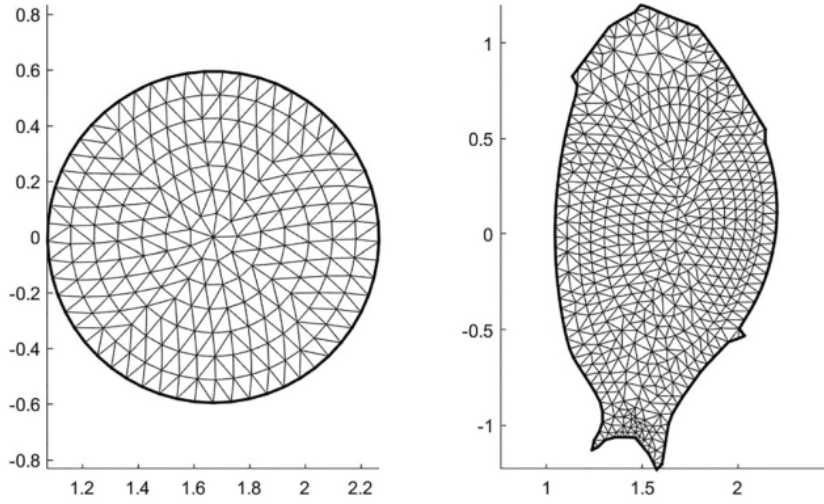
FIGURE 3.1: Representation of the mesh used in TRIMEG, for different geometries. Taken from [24].

ponents are calculated as

$$B_R = -\frac{1}{R}\frac{\partial\psi}{\partial Z}, \quad B_Z = \frac{1}{R}\frac{\partial\psi}{\partial R}, \quad B_\phi = \frac{F}{R}, \tag{3.1}$$

where $\psi = \psi(R, Z)$ is provided in the EQDSK file on (R, Z) grid points and is represented using B-splines in the TRIMEG code. The guiding center equations are the same as Equations 2.33–2.34. The velocities can also be decomposed as

$$\dot{\vec{R}} = v_{\|0} + v_{d0} + v_E, \tag{3.2}$$

$$\dot{v}_\| = \dot{v}_{\|0} + \dot{v}_{\|E}, \tag{3.3}$$

where subscripts 0 and E indicate motion due to the equilibrium, and the electric field respectively. In this work, the electric field is not included, and the drift velocities are calculated as

$$\vec{v}_{d0} \approx \frac{v_\perp^2 + 2v_\|^2}{2\omega_c B}\vec{b} \times \nabla B, \tag{3.4}$$

$$\dot{v}_{\|0} \approx -\mu(b_R\partial_R B + b_Z\partial_Z B), \tag{3.5}$$

where ω_c is the cyclotron frequency, and μ is the magnetic moment. While the higher order $\rho^* = \rho_{th}/a$ terms are ignored in Equations 3.4-3.5, where $\rho_{th} = mv_{th}/(ZeB)$, and a is the minor radius. The complete forms with the ρ^* terms have been implemented recently [25]. In our work, we adopted Equations 3.4-3.5, which is accurate enough for neoclassical studies in typical parameter regimes according to previous theoretical models [12].

TRIMEG Normalization units	
m_N	m_i
R_N	$1\,\mathrm{m}$
T_N	$m_N v_N^2/2$
v_N	$v_{th,i} = \sqrt{\frac{2T_N}{m_N}} = \sqrt{\frac{2T_{i,ref}}{m_i}}$
t_N	$\frac{R_N}{v_N}$
B_N	$1\,\mathrm{T}$

TABLE 3.1: Normalization in TRIMEG [24].

3.1.2 New development in this work and difference from the previous TRIMEG code

For the δf scheme in TRIMEG, the distribution function is represented by the lowest order approximation f_0 and the higher order perturbations δf, namely, $f = f_0 + \delta f$. f_0 is chosen as Maxwellian distribution and δf is obtained from

$$\frac{\mathrm{d}}{\mathrm{d}t}\delta f(t) = -\frac{\mathrm{d}}{\mathrm{d}t}f_0 + C(f,f) \ , \tag{3.6}$$

$$\frac{\mathrm{d}}{\mathrm{d}t} = \frac{\partial}{\partial t} + \dot{\mathbf{R}} \cdot \nabla + \dot{v}_\parallel \frac{\partial}{\partial v_\parallel} \ . \tag{3.7}$$

In this work, the Maxwell distribution is chosen ($f_0 = f_\mathrm{M}$),

$$f_\mathrm{M} = \frac{n_0}{(2T/m)^3 \pi^{3/2}} \exp\left\{ -\frac{mv_\parallel^2}{2T} - \frac{m\mu B}{T} \right\} \ , \tag{3.8}$$

where T and n are functions of the equilibrium magnetic flux, and thus

$$\begin{aligned}
\frac{\mathrm{d}}{\mathrm{d}t} \ln f_\mathrm{M} &= (\mathbf{v}_\parallel + \dot{\mathbf{R}}_d + \delta\dot{\mathbf{R}}) \cdot \left[\vec{\kappa}_n + \left(\frac{mv_\parallel^2}{2T} + \frac{m\mu B}{T} - \frac{3}{2} \right) \vec{\kappa}_T - \frac{m\mu B}{T} \vec{\kappa}_B \right] \\
&\quad - (\dot{v}_{\parallel,0} + \delta\dot{v}_\parallel) \frac{mv_\parallel}{T} \ ,
\end{aligned} \tag{3.9}$$

where $\vec{\kappa}_{n,T,B} \equiv \nabla \ln\{n, T, B\}$, $\dot{\mathbf{R}}_d$ is the magnetic drift velocity, $\delta\dot{\mathbf{R}}$ is the perturbed velocity due to the wave field and the neoclassical electric field, $\dot{v}_{\parallel,0}$ and $\delta\dot{v}_\parallel$ are due to the mirror force and the wave/neoclassical fields, respectively. Furthermore, the perturbed parts $\delta\mathbf{R}$ and $\delta v_\parallel$ contain contributions from the turbulence as well as the radial electric field and can be represented as $\delta\mathbf{R} = \delta\mathbf{R}_{turb} + \delta\mathbf{R}_{E_{nc}}$. For models with $E_r = E_r(r)$, we readily have $\delta\dot{v}_\parallel = 0$,

which is the assumption used in some neoclassical studies [12]. More generally, the neoclassical electric field can vary in the poloidal direction and it is denoted as $E_{nc} = E_{nc}(r, \theta)$

In the previous TRIMEG work [24, 26], the neoclassical effects were ignored, yielding [24]

$$\frac{\mathrm{d}}{\mathrm{d}t} \ln f_{\mathrm{M}} = \delta\dot{\mathbf{R}} \cdot \left[\vec{\kappa}_n + \left(\frac{mv_\parallel^2}{2T} + \frac{m\mu B}{T} - \frac{3}{2} \right) \vec{\kappa}_T - \frac{m\mu B}{T} \vec{\kappa}_B \right] - \delta\dot{v}_\parallel \frac{mv_\parallel}{T} \ . \tag{3.10}$$

For the neoclassical studies in this thesis, we ignore the $n \neq 0$ modes and we have

$$\begin{aligned} \frac{\mathrm{d}}{\mathrm{d}t} \ln f_{\mathrm{M}} &= (\mathbf{v}_\parallel + \dot{\mathbf{R}}_d + \delta\dot{\mathbf{R}}_{E_{nc}}) \cdot \left[\vec{\kappa}_n + \left(\frac{mv_\parallel^2}{2T} + \frac{m\mu B}{T} - \frac{3}{2} \right) \vec{\kappa}_T - \frac{m\mu B}{T} \vec{\kappa}_B \right] \\ &- (\dot{v}_{\parallel,0} + \delta\dot{v}_{\parallel E_{nc}}) \frac{mv_\parallel}{T} \ , \end{aligned} \tag{3.11}$$

where $\delta\dot{\mathrm{R}}_{E_{nc}}$ and $\delta\dot{v}_{\parallel E_{nc}}$ are the perturbed velocity and acceleration due to the neoclassical electric field, respectively. In this work, since we focus on electron transport, E_{nc} is not taken into account, as adopted by previous work [21]. Note that Equations 3.9–3.11 are written in $(\mathbf{R}, v_\parallel, \mu)$ coordinates, for demonstrating the general form of the models without and with neoclassical physics. The right-hand side can be also written in $(\mathbf{R}, E, \mu)$ coordinates, in order to use the constants of motion (E, μ). Furthermore, simplifications, such as no consideration of the electric field, can be adopted to get the implemented equation in TRIMEG in this work, as shown in Equation 3.23 in the next section.

3.2 Diagnosis for axisymmetric components in TRIMEG

In the studies of neoclassical transport, the particle and energy fluxes and the bootstrap current are all axisymmetric variables and need to be calculated numerically. In calculating the variables in configuration space using the markers, three kinds of volumes are used in the following derivation,

- $\Delta\tilde{V}$ for local average which is an infinitesimal volume in all three directions in configuration space;

- $\Delta\hat{V}$ for toroidal average which is a volume with an infinitesimal area in the poloidal cross-section but with the whole toroidal range;

- ΔV for flux surface average which is a volume between two adjacent magnetic flux surfaces.

An important routine implemented in the code during our studies is the flux surface average calculation. For any function F, the flux surface average is [12]

$$\langle F \rangle = \frac{\int_{\Delta V} d^3\vec{R} F}{\int_{\Delta V} d^3\vec{R}} = \frac{d\psi}{dV} \int \frac{dS}{|\nabla\psi|} F, \tag{3.12}$$

where ΔV is the small volume between two adjacent flux surfaces, and dS is the area element on the flux surface. The functions we consider are independent of the toroidal coordinate, hence we can write in general for F

$$F(\psi, \theta) = \frac{\int_{\Delta\hat{V}} d^3\vec{R} \delta f I}{\int_{\Delta\hat{V}} d^3\vec{R}}, \tag{3.13}$$

where $\Delta\hat{V}$ is an arbitrarily small volume element with a small area in the poloidal cross-section but a toroidal width in the whole domain, i.e., $\phi \in [0, 2\pi)$, and the choice of I depends on the function F we are calculating. For example, $I = v_\parallel$ for $F = j_b$. Because $f_m = N/N_{ph} f$, δf can be written as

$$\delta f = \frac{N_{ph}}{N_m} \sum_{p=1}^{N_m} w_p \frac{\delta(\vec{R} - \vec{R}_p)\delta(\vec{v} - \vec{v}_p)}{J_{\vec{R}}}, \tag{3.14}$$

where J is the Jacobian that depends on the specific coordinates used in the model.

For general geometry, we can plug in the definitions and re-write the flux surface average given by Equation 3.12 as

$$\langle F \rangle = \frac{1}{\Delta V} \int_{\Delta V} d^3\vec{R}' \frac{1}{\Delta\hat{V}} \int_{\Delta\hat{V}} d^3\vec{R} \frac{1}{J_{\vec{R}}} \frac{N_{ph}}{N_m} \sum_{p=1}^{N_m} w_p \delta(\vec{R} - \vec{R}_p)\delta(\vec{v} - \vec{v}_p) I, \tag{3.15}$$

after taking the integrals this is simplified to

$$\langle F \rangle = \frac{1}{\Delta V} \frac{N_{ph}}{N_m} \sum_{p \in \Delta V} w_p I_p. \tag{3.16}$$

Note that we can also readily calculate the flux surface average for 3D variables instead of the 2D axisymmetric variable in Equation 3.13, namely,

$$F(\psi, \theta, \phi) = \frac{\int_{\Delta\tilde{V}} d^3\vec{R} \delta f I}{\int_{\Delta\tilde{V}} d^3\vec{R}}, \tag{3.17}$$

where $\Delta\tilde{V}$ is an infinitesimal volume. The flux surface average of F yields the same result in Equation 3.16.

In some cases, the toroidal average is used for the analysis instead of the flux surface average (which is relevant for future applications not using $n = 0$):

$$\langle F \rangle_\phi = \frac{\int_0^{2\pi} d\phi F}{\int_0^{2\pi} d\phi}. \tag{3.18}$$

When plugging in the definitions for F, the average can be written as

$$\langle F \rangle_\phi = \frac{1}{\int_0^{2\pi} d\phi} \frac{1}{\Delta \tilde{V}} \frac{N_{ph}}{N_m} \int_{\Delta \tilde{V}} d^3 \vec{R} \int d\phi \sum_{p=1}^{N_m} w_p \delta(\vec{R} - \vec{R}_p) \delta(\vec{v} - \vec{v}_p) I, \quad (3.19)$$

where if integrals over the toroidal direction and over an arbitrarily small volume are taken, this equation can be rewritten as

$$\langle F \rangle_\phi = \frac{1}{2\pi \Delta \tilde{S}} \Delta \phi \frac{N_{ph}}{N_m} \sum_{p \in \Delta \tilde{S}} \frac{1}{R_p} w_p I_p, \quad (3.20)$$

where $\Delta \tilde{V} = \tilde{R} \Delta \tilde{S} \Delta \phi$ has been adopted.

In our analysis we deal with the flux surface averages normalized by average density, hence if we take into account that $N_{ph} = V_{tot} \langle n \rangle_V$, where V_{tot} is the total volume and $\langle n \rangle$ is the average density in this volume, the flux surface average equation can be rewritten as

$$\frac{\langle F \rangle_\phi}{\langle n \rangle_V} = \frac{1}{2\pi \Delta \tilde{S}} \frac{V_{tot}}{N_m} \sum_{p \in \Delta \tilde{S}} \frac{1}{R_p} w_p I_p, \quad (3.21)$$

where $\Delta \tilde{V} = \Delta \tilde{S} \tilde{R} \Delta \phi$ was used. The values used for analysis in our studies are calculated as

$$\frac{\langle F \rangle_\phi}{\langle n \rangle_V} = \frac{1}{-\bar{e} \frac{n_s}{n_N}} \frac{1}{\Delta \tilde{S}} \underline{\frac{V_{tot}}{2\pi N_m} \left(-\bar{e} \frac{n_s}{n_N}\right) \sum_{p \in \Delta \tilde{S}} \frac{1}{R_p} w_p I_p}, \quad (3.22)$$

where n_s/n_N specifies the number of markers of the species for which the flux is calculated divided by the number of total markers in the simulation, and $\bar{e}$ is the normalized charge for the species. The underlined part in Equation 3.22 has already been implemented in the simulation code, under the subroutine `particle_cls_p2g00`. The flux surface average Eq. 3.16 can be also expressed in the same way. For the calculation of the annulus area in shaped tokamak geometry, the Monte-Carlo integration method is used and the annulus area is calculated at the beginning of the simulation when the markers are distributed uniformly.

3.3 Implemented Physical model

3.3.1 Implemented Equations and normalizations

For our neoclassical studies, the TRIMEG code was modified as described in this section. In addition to the discussions in 3.1.2, the δf model was adopted and a weight equation was implemented as given by Equation 2.84 in our (R, Z, ϕ) coordinates

$$\frac{dw}{dt} = (1 - w)(\vec{v}_d \cdot \vec{\kappa}) = (1 - w)(v_{d,R} \kappa_R + v_{d,Z} \kappa_Z), \quad (3.23)$$

where κ is the negative gradient of the equilibrium distribution function given by

$$\vec{\kappa} = -\frac{d \ln f_0}{d\vec{x}} = -\left(\frac{d \ln f_0}{dn}\frac{dn}{dR} + \frac{d \ln f_0}{dT}\frac{dT}{dR}\right)\hat{R} - \left(\frac{d \ln f_0}{dn}\frac{dn}{dZ} + \frac{d \ln f_0}{dT}\frac{dT}{dZ}\right)\hat{Z}$$
$$= -\left(\frac{d \ln n}{dR} + \left(\frac{mv^2}{2T} - \frac{3}{2}\right)\frac{d \ln T}{dR}\right)\hat{R} - \left(\frac{d \ln n}{dZ} + \left(\frac{mv^2}{2T} - \frac{3}{2}\right)\frac{d \ln T}{dZ}\right)\hat{Z}.$$
$$(3.24)$$

Taking into account the normalization given in table 3.1, the normalized equation implemented in the code is

$$\frac{dw}{dt} = (1-w)(-\bar{v}_{d,R}\left(\frac{d \ln n}{dR} + \left(\frac{\bar{m}\bar{v}_\parallel^2}{\bar{T}} + \frac{2\bar{\mu}\bar{m}\bar{B}}{\bar{T}} - \frac{3}{2}\right)\frac{d \ln T}{dR}\right)$$
$$-\bar{v}_{d,Z}\left(\frac{d \ln n}{dZ} + \left(\frac{\bar{m}\bar{v}_\parallel^2}{\bar{T}} + \frac{2\bar{\mu}\bar{m}\bar{B}}{\bar{T}} - \frac{3}{2}\right)\frac{d \ln T}{dZ}\right).$$
$$(3.25)$$

To take into account the collisional effects, the discretized Lorentz collision operator given by Equation 2.96 is implemented in the code,

$$\xi = \xi_0(1 - \bar{\nu}\Delta t) + (R - 0.5)[12(1 - \xi_0^2)\bar{\nu}\Delta t]^{1/2}, \qquad (3.26)$$

where ξ is the particle pitch as defined earlier, and $\bar{\nu} = \nu t_N$ is the normalized collision frequency. Furthermore, regardless of the choice of $\bar{\nu}\Delta t$, due to the choice of R being random, $|\xi|$ can become greater than 1, as shown in Figure 3.2. This would cause a nonphysical solution with $|v_\parallel/v| > 1$, which was fixed by re-setting $|\xi|$ equal to exactly 1 in those cases. For large values of $\bar{\nu}\Delta t(> 0.5)$, more markers end up with $|\xi| > 1$ after the collision, and the re-setting operation is needed. For small values of $\bar{\nu}\Delta t(< 0.1)$, only a small portion of markers enter the $|\xi| > 1$ zone, and the re-setting operation is needed less frequently. In the simulations, the value for $\bar{\nu}\Delta t$ is chosen to be less than 0.1 to avoid frequent use of re-setting.

3.3.2   Diagnosis and benchmark using the local neoclassical transport theory

The benchmark is done by comparing the simulation results to the theoretical local electron transport model [12, 21]. We can also write simplified equations for electrons in a circular geometry, where ion charge is equal to one, and assuming constant pressure and temperature for the ion species. From the
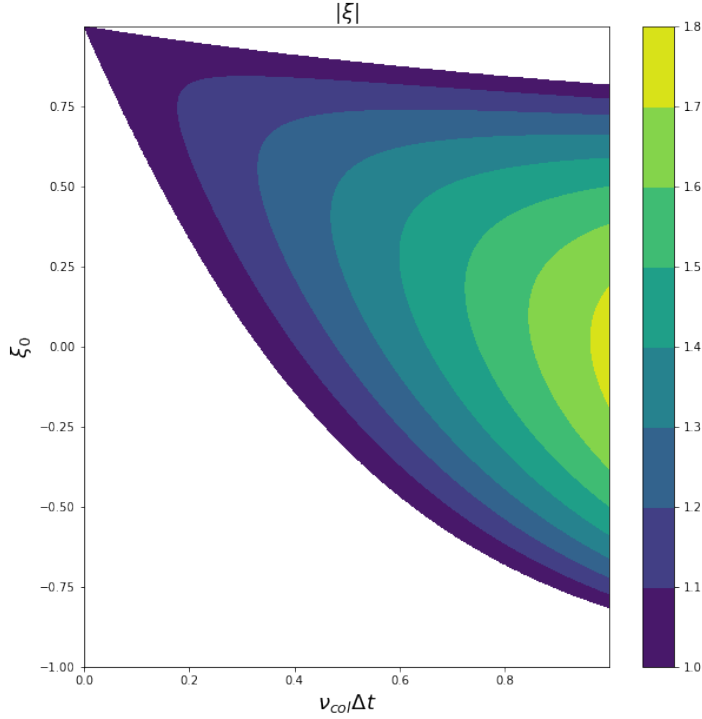
FIGURE 3.2: Values of ξ_0 and $\nu\Delta t$ when ξ becomes larger than 1, during evolution using the Lorentz collision operator given in Equation 2.96. Here the random number R is taken to be 0.9, and ν_{col} represents the normalized collision frequency.

discussions in section 2.2.4, we can write these equations as follows

$$A'_{1e} = \frac{\partial \ln n_e}{\partial r} - \frac{3}{2}\frac{\partial \ln T_e}{\partial r}, \tag{3.27}$$

$$\Gamma_e = -n_e \frac{4}{3\sqrt{\pi}}\nu_{ei}\epsilon^{-3/2}\rho^2 q^2 \left(K_{11}A'_{1e} + K_{12}\frac{\partial \ln T_e}{\partial r} \right), \tag{3.28}$$

$$q_e = -n_e T_e \frac{4}{3\sqrt{\pi}}\nu_{ei}\epsilon^{-3/2}\rho^2 q^2 \left(K_{12}A'_{1e} + K_{22}\frac{\partial \ln T_e}{\partial r} \right)$$

$$- \frac{5}{2}T_e\Gamma_e, \tag{3.29}$$

$$\left\langle (J_\| - J_{\|s})/h \right\rangle = -n_e \frac{T_e}{m_e v_{th,e}}e\epsilon^{-1/2}\rho q \left(K_{13}A'_{1e} + K_{23}\frac{\partial \ln T_e}{\partial r} \right), \tag{3.30}$$

where the dimensionless K coefficients are also given in Equations 2.69-2.70 and using values for the numerical coefficients for charge number equal to 1

[12]:

$$K_{11} = 1.04 \left(\frac{1}{1 + 2.01\nu_{*e}^{1/2} + 1.53\nu_{*e}} + \frac{\epsilon^{3/2}(0.89^2/1.53)\nu_{*e}\epsilon^{3/2}}{1 + 0.89\nu_{*e}\epsilon^{3/2}} \right), \qquad (3.31)$$

$$K_{12} = 1.20 \left(\frac{1}{1 + 0.76\nu_{*e}^{1/2} + 0.67\nu_{*e}} + \frac{\epsilon^{3/2}(0.56^2/0.67)\nu_{*e}\epsilon^{3/2}}{1 + 0.56\nu_{*e}\epsilon^{3/2}} \right), \qquad (3.32)$$

$$K_{22} = 2.55 \left(\frac{1}{1 + 0.45\nu_{*e}^{1/2} + 0.43\nu_{*e}} + \frac{\epsilon^{3/2}(0.43^2/0.43)\nu_{*e}\epsilon^{3/2}}{1 + 0.43\nu_{*e}\epsilon^{3/2}} \right), \qquad (3.33)$$

$$K_{13} = 2.3[1 + 1.02\nu_{*e}^{1/2} + 1.07\nu_{*e}]^{-1}[1 + 1.07\nu_{*e}\epsilon^{3/2}]^{-1}, \qquad (3.34)$$

$$K_{23} = 4.19[1 + 0.57\nu_{*e}^{1/2} + 0.61\nu_{*e}]^{-1}[1 + 0.61\nu_{*e}\epsilon^{3/2}]^{-1}, \qquad (3.35)$$

$$K_{33} = 1.83[1 + 0.68\nu_{*e}^{1/2} + 0.32\nu_{*e}]^{-1}[1 + 0.66\nu_{*e}\epsilon^{3/2}]^{-1}. \qquad (3.36)$$

The normalized equations used in diagnostics are

$$\bar{A}'_{1e} = \frac{A'_{1e}}{R_N} = A'_{1e}, \qquad (3.37a)$$

$$\bar{\Gamma}_e = \frac{\Gamma_e}{nv_N} = -\frac{4}{3\sqrt{\pi}}\bar{\nu}_{ei}\epsilon^{-3/2}\rho^2 q^2 \left(K_{11}A'_{1e} + K_{12}\frac{\partial \ln T_e}{\partial r} \right), \qquad (3.37b)$$

$$\bar{q}_e = \frac{q_e}{nv_N m_N v_N^2} = -\frac{1}{2}\frac{4}{3\sqrt{\pi}}\bar{\nu}_{ei}\epsilon^{-3/2}\rho^2 q^2 \left(K_{12}A'_{1e} + K_{22}\frac{\partial \ln T_e}{\partial r} \right) - \frac{5}{4}\bar{\Gamma}_e, \qquad (3.37c)$$

$$\bar{j}_b = \frac{j_b}{e_i nv_N} = \frac{1}{2}\sqrt{\frac{m_i}{m_e}}\epsilon^{-1/2}\rho q \left(K_{13}A'_{1e} + K_{23}\frac{\partial \ln T_e}{\partial r} \right), \qquad (3.37d)$$

where the normalized quantities are denoted by a bar over the variables, and $\langle (J_\parallel - J_{\parallel s})/h \rangle \equiv j_b$. In the asymptotic limits of collisionality, these formulas can also be re-written as described in the paper by Lin [21]. For the banana regime, we go to the limit of $\nu \to 0$. We get the following analytical equations for particle flux Γ, energy flux Q, and the bootstrap current j_b [21]:

$$\Gamma = \langle \int d^3 v v_{dr} f_1 \rangle = \frac{3}{8}I_1\nu\rho^2\frac{q^2}{\epsilon^2}n(\kappa_n + \kappa_t),$$

$$Q = \langle \int d^3 v \frac{1}{2}mv^2 v_{dr} f_1 \rangle = \frac{5T}{2}\left(\Gamma + \frac{3}{8}I_1\nu\rho^2\frac{q^2}{\epsilon^2}n\kappa_T \right), \qquad (3.38)$$

$$j_b = \langle \int d^3 v \frac{v_\parallel}{h} f_1 \rangle = \frac{3}{4}I_3\frac{c}{B_{p0}}\frac{dp}{dr},$$

where $\langle ... \rangle \equiv \int_0^{2\pi} h d\theta/(2\pi)$ represents the flux surface average. Additionally, $\epsilon = r/R_0$, $h \equiv 1 + \epsilon\cos\theta$, $\rho = mv_{th,e}c/eB_0$, $q = rB_0/(R_0 B_{p0})$, $p = (3/2)nT$, and to the lowest order in ϵ,

$$I_1 = I_3 = 1.38\sqrt{2\epsilon}. \qquad (3.39)$$

For the collisional limit we go to the limit $\nu \to \infty$ and get the following analytical solutions [21]

$$\begin{aligned}
\Gamma &= \nu q^2 \rho^2 n (\kappa_n + \kappa_T), \\
Q &= \frac{5T}{2}(\Gamma + \nu q^2 \rho^2 n \kappa_T).
\end{aligned} \tag{3.40}$$

The normalized form of the fluxes and bootstrap current are as follows, for the banana regime,

$$\bar{\Gamma} = \frac{\Gamma}{n v_N} = \frac{3}{8} I_1 \bar{\nu} \rho^2 \frac{q^2}{\epsilon^2}(\kappa_n + \kappa_T), \tag{3.41}$$

$$\bar{Q} = \frac{Q}{n v_N m_N v_N^2} = \frac{5}{2}\frac{T_e}{m_N v_N^2}\left(\bar{\Gamma} + \frac{3}{8} I_1 \bar{\nu} \rho^2 \frac{q^2}{\epsilon^2}\kappa_T\right), \tag{3.42}$$

$$\bar{j}_b = \frac{j_b}{e_i n v_N} = \frac{9}{16}\sqrt{\frac{m_i}{m_e}} I_3 \rho \frac{q}{\epsilon}(\kappa_T + \kappa_n). \tag{3.43}$$

For the collisional regime,

$$\bar{\Gamma} = \bar{\nu} q^2 \rho^2 (\kappa_n + \kappa_T), \tag{3.44}$$

$$\bar{Q} = \frac{5}{2}\frac{T_e}{m_i v_{th,i}^2}\left(\bar{\Gamma} + \bar{\nu} q^2 \rho^2 \kappa_T\right), \tag{3.45}$$

where $\bar{\nu} = \nu t_N$ represents the normalized collision frequency. Comparisons to the simulation results are done by calculating values using the flux surface average methods described in section 3.2 during the simulation, where the values for I are chosen as $I = v_r m v^2/2$ for the energy flux, and $I = v_r$ for the particle flux, where v_r is the radial drift velocity. The analytical formulas described in this chapter are implemented in the Matlab scripts, where we are taking the average values of q and κ_n for the flux surfaces, and in the Fortran code, where the values for κ_n and q are taken for each grid point locally. These results are described in sections 4.1-4.5.

Overall, the analytical expressions for the fluxes were added to the code, in addition to the weight equation, collision operator, and the bootstrap current as well as the particle and energy flux calculations.

Chapter 4

Results of Neoclassical Electron transport and bootstrap current

4.1 Benchmark of the local electron transport model

We first try to reproduce results of an earlier work [21], where a single flux surface was considered to study the neoclassical transport of electrons. We simulate a finite width annulus using the ad hoc equilibrium, assuming magnetic surfaces to be concentric and circular, using the Matlab version of TRIMEG-GKX. We use the same parameters in our simulation taking into account the difference in normalization. In the mentioned paper, the normalization used is the gyro-kinetic normalization, also shown in Table 4.1. However, for simulating the annulus we use the normalization given in table 4.2.

Furthermore, as we are dealing with circular geometry we can rewrite the flux

Gyrokinetic Normalization units	
m_{NG}	m_i
R_{NG}	$\rho_s = \sqrt{\frac{T_e}{m_i}}\frac{m_i}{eB_0}(T_e = T_i, \rho_s = \frac{\sqrt{T_i m_i}}{eB_0} = \frac{\rho_{th,i}}{\sqrt{2}})$
T_{NG}	$T_e(= T_i)$
v_{NG}	$v_{th,i} = \sqrt{\frac{2T_N}{m_N}} = \sqrt{\frac{2T_i}{m_i}}$

TABLE 4.1: Gyrokinetic Normalization used in [21].

Normalization units used in benchmark	
m_N	m_e
R_N	$1m$
T_N	$2T_e(=2T_i)$
v_N	$v_{th,e} = \sqrt{\frac{T_N}{m_N}} = \sqrt{\frac{2T_e}{m_e}}$

TABLE 4.2: Normalization used for benchmark.

surface calculation for some functions $F(r, \theta)$ as:

$$\langle F \rangle = \frac{1}{4\pi^2 R_0 r} \int_0^{2\pi} d\phi \int_0^{2\pi} d\theta\, r R F = \frac{1}{2\pi} \int_0^{2\pi} d\theta\, h F, \qquad (4.1)$$

where $h \equiv 1 + r/R_0 cos\theta$.

We obtained the result of of our scan given in Figure 4.1, where the scanned parameter is $\nu^* = \epsilon^{-3/2}\nu\sqrt{2}qR_0/v_{th}$, also given in Equation 2.41. The simulation results are compared to the analytical theory [12], and the exact equations are also described in section 3.3.2. Furthermore, to avoid the high levels of noise in the later parts of the simulation, the values for the energy and particle flux are taken after 15 transit periods. Looking at the equations for the flux calculations, the particle and energy fluxes need less time to saturate than the bootstrap current, as the radial drift is constant, and the change of the perpendicular velocity distribution is mostly due to the radial transport which is small. However, for the bootstrap current, as discussed in the background section 2.2.3, with collisions the parallel velocity distribution function changes until saturation which is the cause of the bootstrap current. The collision frequency determines the speed of this change, hence the bootstrap current saturation is slower than the fluxes associated with the radial drift velocity. To investigate the differences, we can look at the signal to noise ratios for different values of ν^*.

As the difference between analytical and simulation results are somewhat high for the banana regime limit, we can look at the time evolution of the fluxes given in Figure 4.2 to investigate why. We can see that the time to reach the saturated results for the bootstrap current is few thousand transit periods, and the fluctuations in the fluxes are increasing in time. If we look at Figure 4.3, we can see that the noise is increasing to become few magnitudes of the signal, hence why we are taking the values for the particle flux and the energy flux at the first few transit periods. Therefore, the cause for the difference between analytical solution and the simulation results is most likely the high noise level accumulated during the simulation time.

If we look at the plateau regime, given in Figure 4.4, the noise levels are much smaller and the agreement between the simulation results and the analytical
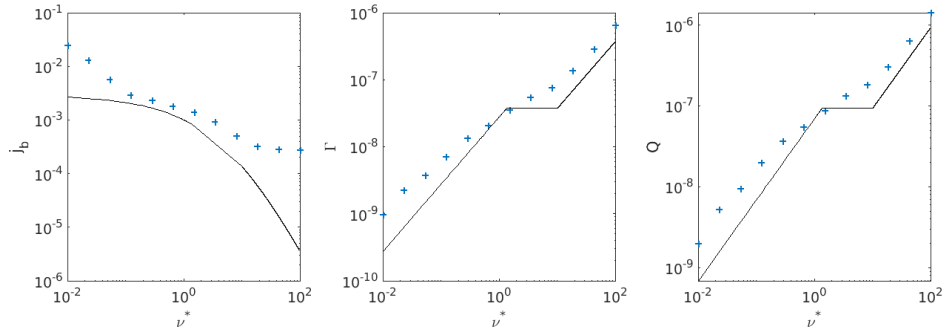
FIGURE 4.1: Simulation for ad hoc equilibrium in finite width annulus, using same parameters as [21], and ν^* is given in Equation 2.41. j_b, Γ, and Q are the normalized values for particle flux, bootstrap current, and energy flux respectively. The number of markers used is 10^5. The range of $\nu^* < 1$ corresponds to the banana regime, $1 < \nu^* < 10$ to the plateau regime, and $10 < \nu^*$ to the collisional regime. Due to high signal to noise ratio, the values for particle flux and energy flux were taken at $t = 15 \cdot T_{tr}$ for low collision frequency cases, or at $t = 10 \cdot T_{tr}$ for high collision frequencies.

solutions are also much better.

For the collisional regime, given in Figure 4.5, we also observe high oscillations in the bootstrap current, which could be the reason for the large difference in the analytical solutions and the simulation.

Overall, we observe very high noise level and the next step is to use the TRIMEG-C0 version of the code in Fortran, which is capable to simulate larger number of markers in the whole volume of the Tokamak, this will decrease the noise levels and produce better agreement between theory and the simulation.
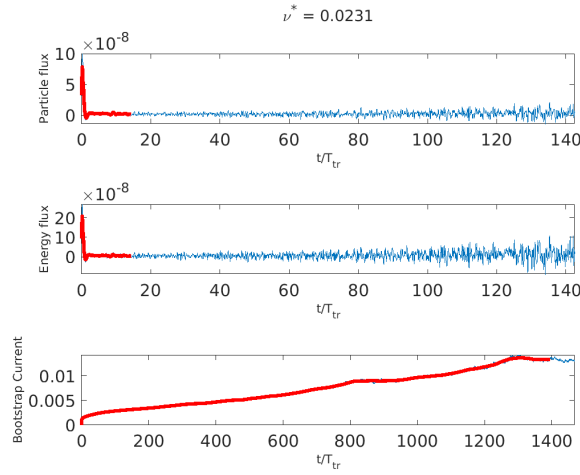
FIGURE 4.2: Time evolution of fluxes in the banana regime, for the simulation of a finite width annulus, using same parameters as [21], and ν^* is given in Equation 2.41. The number of markers used is 10^5. The red lines represent the smoothed data using a moving average filter with a window size of 10% of the total data points. Due to high signal to noise ratio, the values for particle flux and energy flux were taken at $t = 15 \cdot T_{tr}$ for low collision frequency cases, or at $t = 10 \cdot T_{tr}$ for high collision frequencies.
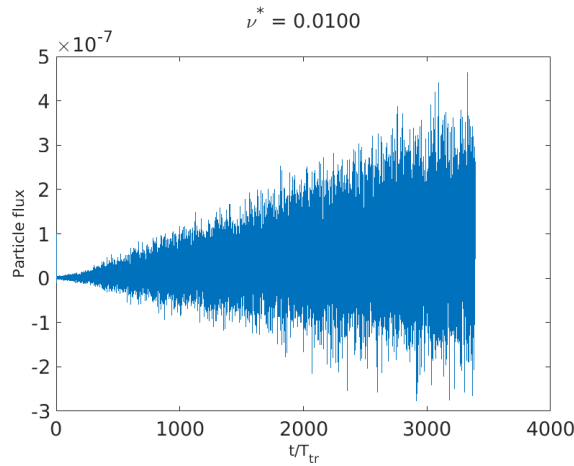
FIGURE 4.3: Time evolution of the particle flux Γ for the simulation of a finite width annulus, using same parameters as [21], and ν^* is given in Equation 2.41. The number of markers used is 10^5.
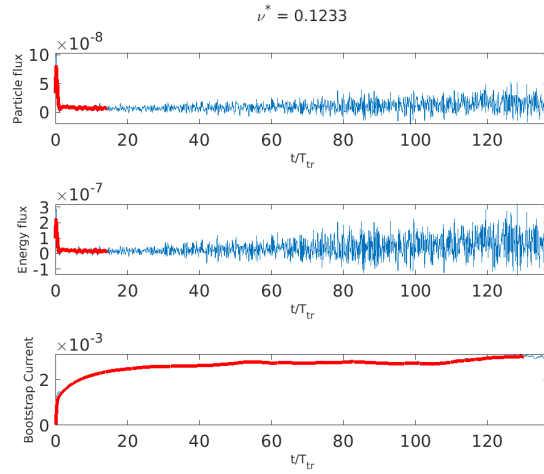
FIGURE 4.4: Time evolution of fluxes in the plateau regime, for the simulation of a finite width annulus, using same parameters as [21], and ν^* is given in Equation 2.41. The number of markers used is 10^5. The red lines represent the smoothed data using a moving average filter with a window size of 10% of the total data points.
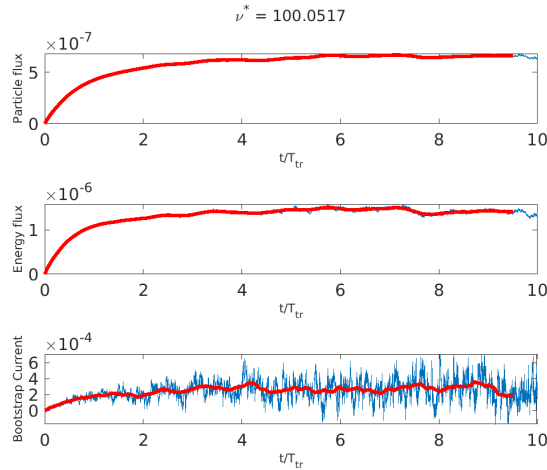
FIGURE 4.5: Time evolution of fluxes in the collisional regime, for the simulation of a finite width annulus, using same parameters as [21], and ν^* is given in Equation 2.41. The number of markers used is 10^5. The red lines represent the smoothed data using a moving average filter with a window size of 10% of the total data points.

4.2 Convergence studies in TRIMEG-C0 (the unstructured mesh version in Fortran)

The numerical verification of the implemented collision operator and resulting neoclassical physics in the TRIMEG C0 version is discussed here. We are now simulating the full torus geometry and no longer a fixed-width annulus. The dependence of the results on the different parameters of the simulation such as the time step size, marker number, and the ways of averaging the results is discussed. In this section, all the cases considered are run using the "Cyclone profiles" which are described in the next section.

4.2.1 The convergence of the net fluxes and current

We start by analyzing the net fluxes and current for testing the convergence. The case considered here is described in more detail in section 4.4. Looking at a 2D picture of the fluxes given in Figure 4.6, we see the flux value at each grid point. For the current analysis we add up values for all the grid points and look at the changes for the net fluxes and in the next section we consider the changes in the flux surface averaged values. We start with the consideration of the marker numbers, given in Figure 4.7. We see that the time it takes to reach saturation is independent of the number of markers although the noise levels are significantly different. However, if the number of markers is 10^5 instead of 10^6, the difference in the fluxes is in the order of 10^2, hence it is important during the simulation to not have too few markers. Furthermore, the behaviour is the same if we consider high collisionality cases, as seen in Figures 4.9-4.10.
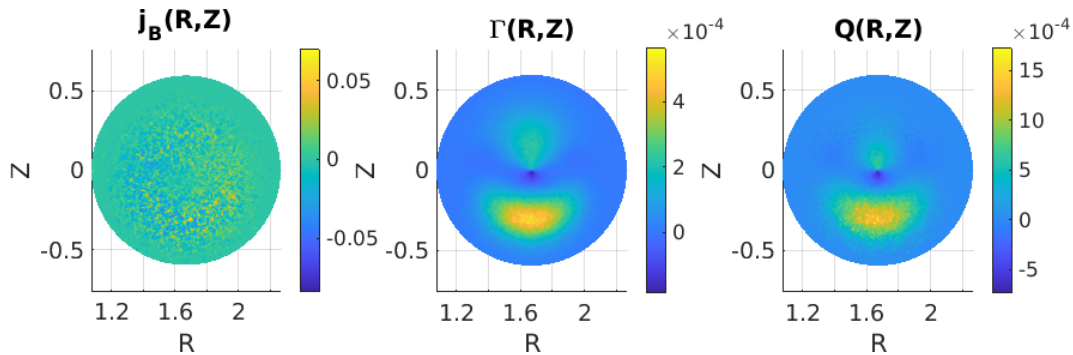
FIGURE 4.6: (R,Z) cross-section of the TRIMEG-C0 simulation of the bootstrap current and fluxes, using 10^7 markers for 20 transit periods, cyclone equilibrium profiles, and $\bar{\nu} = 318$.

Another important parameter to consider when running simulations is the time-step size. The ideal choice would be as large as possible, to be able to run longer simulations. However, for large values of it, the simulation results
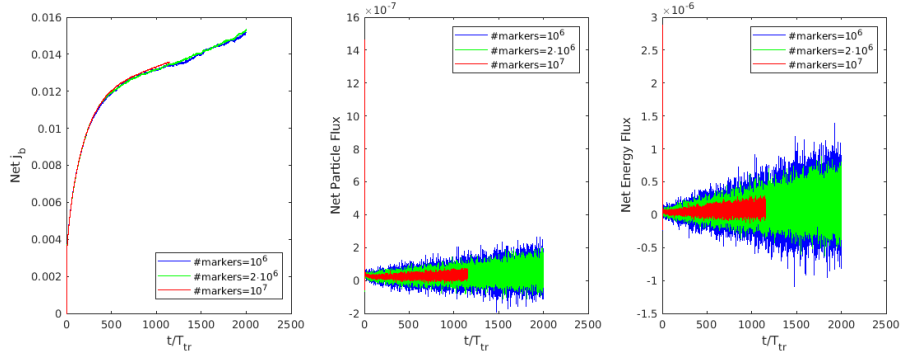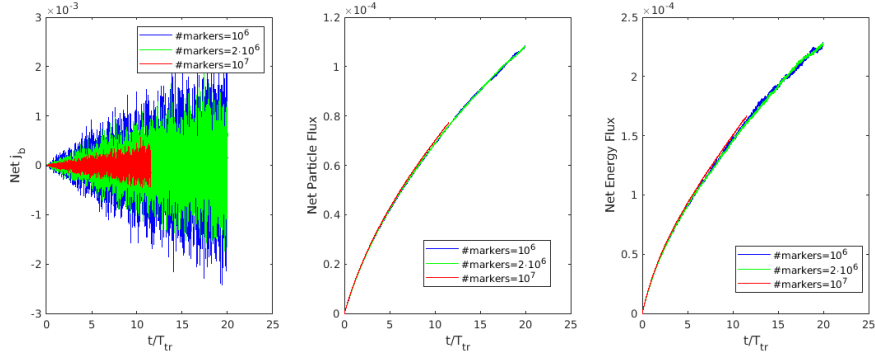
FIGURE 4.7: Dependence of net bootstrap current and net fluxes, on the number of markers used for the simulation. The time-step size is $0.05/T_{tr}$, and $\bar{\nu} = 0.003$.
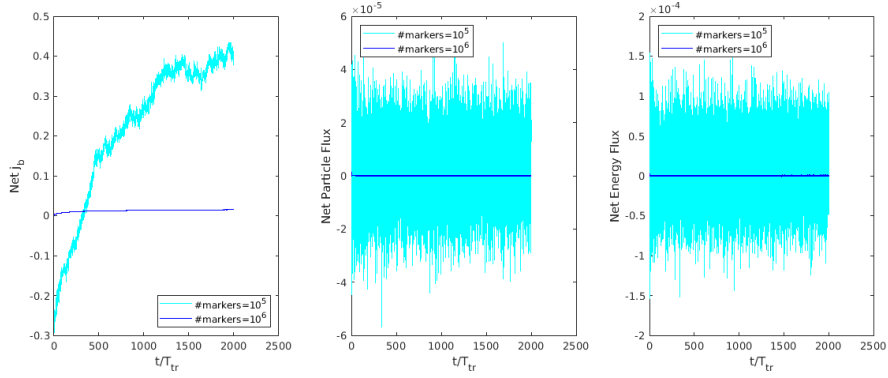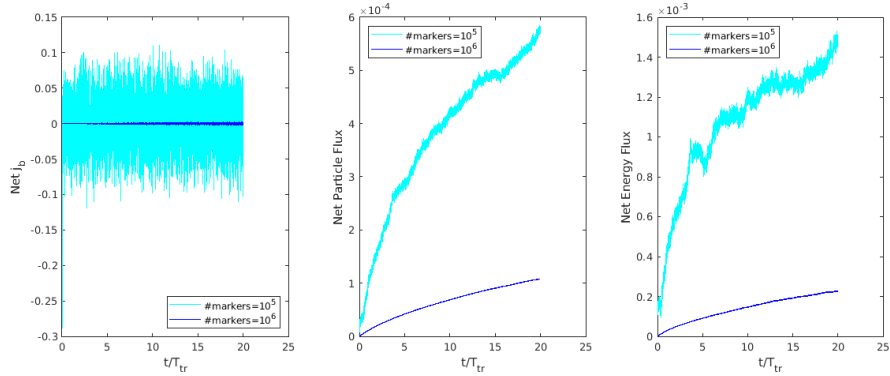

FIGURE 4.8: Dependence of net bootstrap current and net fluxes, on the number of markers used for the simulation, with same parameters as Figure 4.7, but for different number of markers. Similarly, the time-step size is $0.05/T_{tr}$, and $\bar{\nu} = 0.003$.

are no longer physical. Considering a case when the collision frequency is small, as seen on Figure 4.11, we observe that for large time-step size, the markers accumulate in the center of the grid. As for the collisional case, if the time-step size is very large, the particles leave the simulation grid fairly soon, which is the expected behaviour in the high collision case. Considering a single particle, if the random number in the collision operator becomes 1, the parallel velocity could also be converted to the perpendicular velocity, hence the particle would have a very large radial velocity and could drift outside of the simulation domain in a single step of the random walk. Furthermore, as we are considering small angle collisions, when the collision operator is applied, the change in the pitch needs to be small so that we have small angle collisions. As seen from Equation 2.96, the quantity $\nu\Delta t$ determines the magnitude of the change in the pitch and needs to be sufficiently small to stay in the small angle scattering limit.

FIGURE 4.9: Dependence of net bootstrap current and net fluxes, on the number of markers used for the simulation. The time-step size is $0.0005/T_{tr}$, and $\bar{\nu} = 318$.

FIGURE 4.10: Dependence of net bootstrap current and net fluxes, on the number of markers used for the simulation, with same parameters as Figure 4.9, but for different number of markers. Similarly, the time-step size is $0.0005/T_{tr}$, and $\bar{\nu} = 318$.

4.2.2 The convergence of the flux surface averaged fluxes and current

As the analytical values are calculated for the flux surface averaged fluxes, it is important to also analyse the convergence of these profiles from the particle simulations. The important parameters for this convergence study are also the particle number, as well as the method of the flux surface average. The radial profiles of the bootstrap current and the fluxes are visualized and compared among cases with different values of the marker numbers. Two sets of cases are studied. For the high collisionality case, $\bar{\nu} \approx 300$ the results are shown in Figure 4.13. As the marker number is equal to or larger than 10^6, the radial profiles start to converge. The low collision case with $\bar{\nu} \approx 0.003$, is also analysed. Good convergence of the fluxes is also observed as the marker number is equal to or larger than 10^6. For the bootstrap current, the physical values are low according to the theoretical results [12] and thus the noise-to-
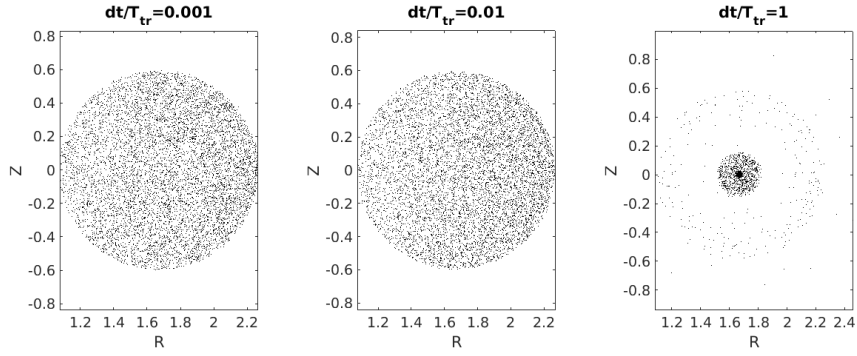
FIGURE 4.11: Distribution in space for randomly picked 7812 markers out of 10^6 used during the simulation, for different values of time-step size dt. For all figures the number of time-steps is 5000, and $\bar{\nu} = 0.003$.
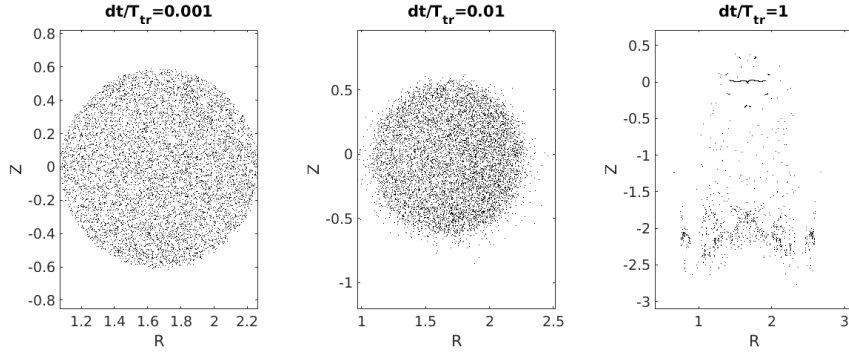
FIGURE 4.12: Distribution in space for randomly picked 7812 markers out of 10^6 used during the simulation, for different values of time-step size dt. For all figures the number of time-steps is 5000, and $\bar{\nu} = 318$.

signal ratio in the particle simulation is high, which leads to worse convergence of the bootstrap current compared to the other quantities. The convergence can be improved by further increasing the marker number or using a longer time evolution average, as we adopted in the following chapters.
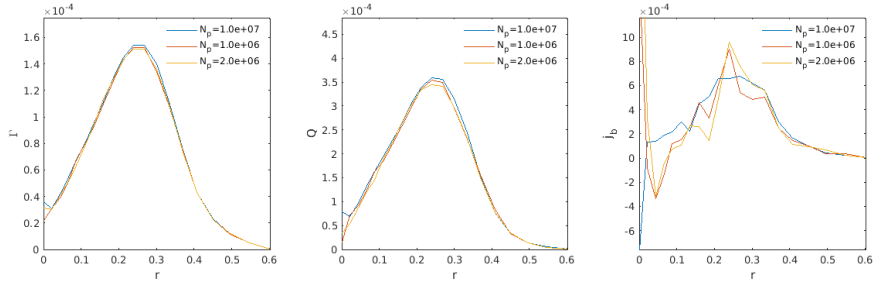
FIGURE 4.13: The particle and the energy fluxes as well as the bootstrap current for different values of the marker number. This is a high collision frequency case with $\bar{\nu} \approx 300$.
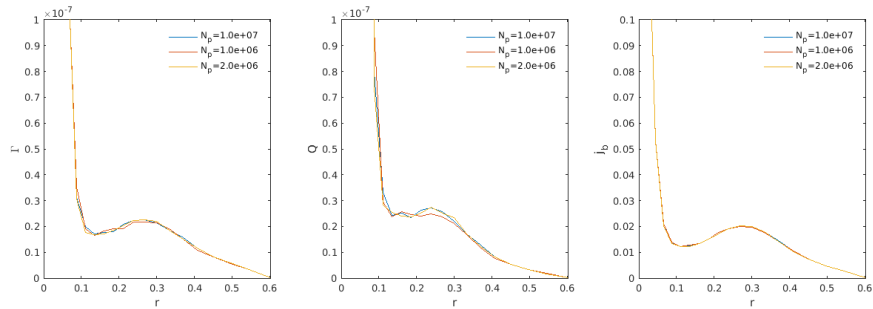
FIGURE 4.14: The particle and the energy fluxes as well as the bootstrap current for different values of the marker number. This is a low collision frequency case with $\bar{\nu} \approx 0.003$.

4.3   Electron transport results for the larger aspect ratio case

In this section, we will consider the International Tokamak Physics Activity (ITPA) case, which has been defined in the benchmark of the Toroidal Alfvén Eigenmode (TAE) driven by energetic particles (EPs) [15]. This is a Tokamak plasma featured by a large aspect ratio $a/R_0 = 1/10$ and concentric circular magnetic surfaces. The on-axis magnetic field is $3\,\mathrm{T}$. The major radius $R_0 = 10\,\mathrm{m}$. The nominal safety factor is $q = 1.71 + 0.16(r/a)^2$, featured by low magnetic shear. In generating the EQDSK file for the ad-hoc equilibrium, the analytical form is adopted,

$$\bar{q} = \bar{q}_0 + \bar{q}_2 r^2 \quad , \tag{4.2}$$

where $\bar{q} = q\sqrt{1 - r^2/R_0^2}$. A simplified match to the q profile is adopted by letting

$$\bar{q}_0 = q_0 = 1.71 \quad , \quad \bar{q}_2 = q_2 = 0.16 \quad , \tag{4.3}$$

which is a good approximation in the moderate to large aspect ratio. Note that the 1D q profile is shown along the radial-like coordinate $\sqrt{\psi}$, where ψ is the normalized poloidal magnetic flux. The magnetic field and the q profile are visualized in Figure 4.15.
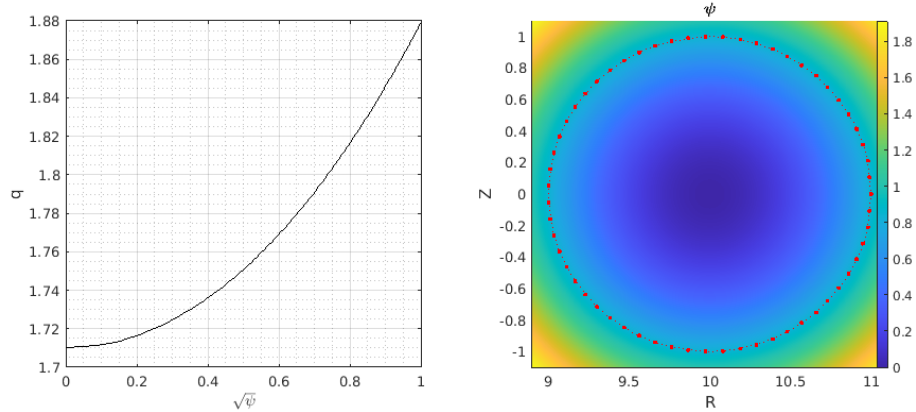
FIGURE 4.15: The q profiles (left) and poloidal magnetic flux map (right) of the ITPA large aspect ratio case.

In our study of neoclassical transport and bootstrap current generation, we only keep the electrons as the kinetic species and adopt uniform electron temperature. The electron density gradient is nonuniform and the following profile

is adopted in solving the weight Equation [26]

$$n_e(r) = n_{e,0} c_3 \exp\left(-\frac{c_2}{c_1}\tanh\frac{r-c_0}{c_2}\right) \ , \tag{4.4}$$

$$\frac{d\ln n_e}{dr} = -\frac{1}{c_1}\left[1 - \tanh^2\frac{r-c_0}{c_2}\right] \ , \tag{4.5}$$

where $c_0 = 0.49123$, $c_1 = 0.298228$, $c_2 = 0.198739$, and $c_3 = 0.521298$. In the original benchmark study, this density profile is used as the EP density while in our work, we use it as the electron density. The density profile and its gradients are visualized in Figure 4.16.
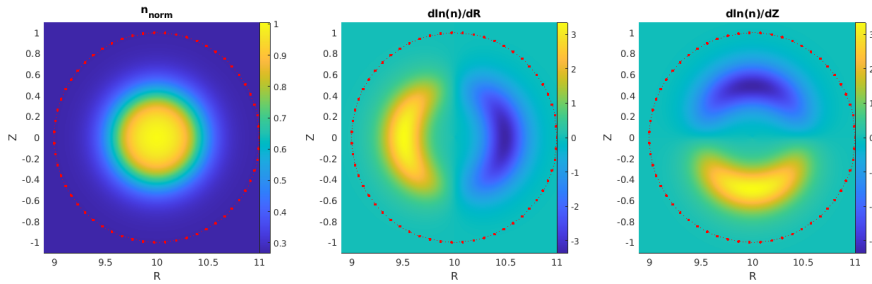
FIGURE 4.16: The density profile for ITPA large aspect ratio case.

We simulate cases with high and low collision frequencies and compare the results with the local theory. During the simulation, the density profile changes gradually because of the particle transport due to collisions. At the end of the simulation, the density profiles are analyzed, as can be seen in Figure 4.17. For the high collision case, the density change is of the order of 1%, while for the low collision case, $|\delta n| < 0.4\%$. This density variation has negligible effects on the density gradient as given in Equations 4.16 with the chosen coefficients and thus the particle/energy fluxes and the bootstrap current stay at the same level after a ramp-up phase until the end of the simulations. The radial profiles of the particle flux, energy flux, and bootstrap current are also analyzed, as shown in Figures 4.18-4.19. For the low collision frequency limit, we observe good agreement between the theoretical calculation and the simulation, as seen in Figure 4.18. The red lines for the particle flux and energy flux indicate solutions in the low collisionality limit given by Equations 3.41-3.42, while the blue lines are in the high collisionality limit given by Equations 3.44-3.45. As for the bootstrap current, the blue line indicates the low collision limit given by Equation 3.43, and the red line is given by the analytical formula by Hinton which takes into account finite collision frequency given in Equation 3.37. We observe a big difference in the energy and particle flux near the axis for low collisionality. The reason is that the theoretical results do not apply near the axis since the theoretical formulae Equations 3.41-3.42 give infinite particle and energy fluxes for $r = 0$. The discrepancy between the theory and the
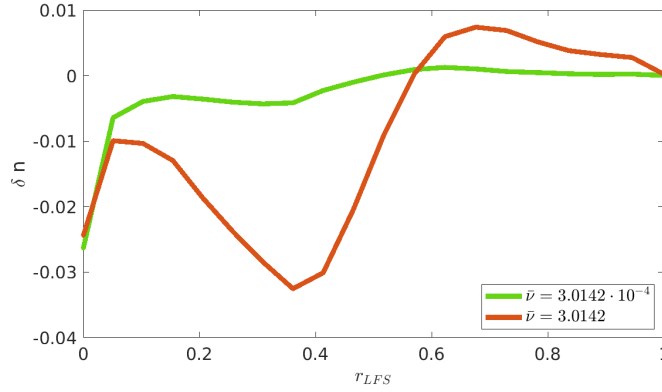
FIGURE 4.17: The radial profiles of the density change at the end of the simulation, where r_{LFS} is the radial coordinate from the axis to the direction of the low field side.

simulation is also observed in the study of ion transport in previous work [22]. The particle simulation is more powerful in the sense that it also applies near the axis.

As for the high collisionality case, the results are given in Figure 4.19. For the particle flux and the energy flux, we have a very good agreement with the analytical solutions. However, the bootstrap current seems to have about the same magnitude but not a definite shape, which might be due to the high noise-to-signal ratio. Increasing the marker number can improve the quality of the bootstrap current but is not of our interest due to the low magnitude of the current in the collisional limit.
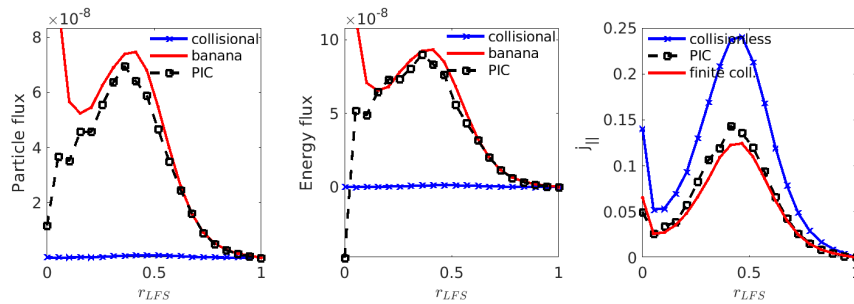
FIGURE 4.18: The radial profiles of the particle flux, energy flux, and the bootstrap current for the low collision frequency case, where $\bar{\nu} \approx 3 \cdot 10^{-5}$. The dashed lines represent the simulation result, while the blue and red lines represent the analytical solutions.

We also investigate the fluxes and bootstrap current as a function of the collision frequency as shown in Figure 4.20. The reference radial location was chosen close to where the maximum values of fluxes were reached ($r \approx 0.23$), and
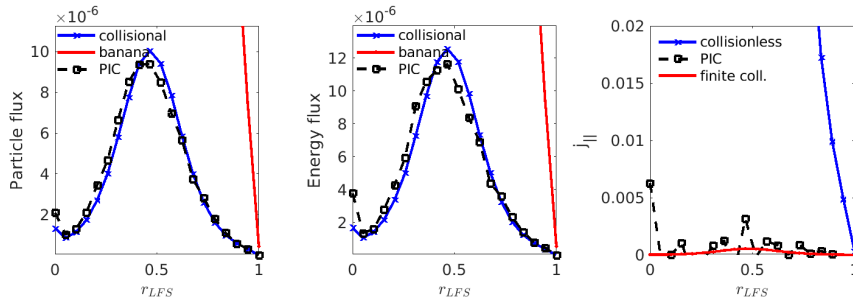
FIGURE 4.19: The radial profiles of the particle flux, energy flux, and the bootstrap current for the high collision frequency case, where $\bar{\nu} \approx 3$. The dashed lines represent the simulation result, while the blue and red lines represent the analytical solutions.

the fluxes and the current are compared with the values from the theoretical radial profile at this reference location. We observe that the bootstrap current from simulations decreases much faster as collision increases in the plateau and the collisional regimes than expected from the analytical interpolation solution. However, we observe good agreement for the particle and energy fluxes with the analytical solutions, in the low ($\nu^* < 1$) and high ($\nu^* > 10$) collisionality limits. Furthermore, the plateau ($1 < \nu^* < 10$) regime is also visible where the fluxes stay almost constant for different collision frequencies, and the overall behavior is qualitatively consistent with previous results [12, 21]. For the bootstrap current, the lowest collision frequency case does not produce the highest current as would be expected. Similar to the Cyclone case, which we will study in the next section, this is due to the bootstrap current still increasing slightly when the simulation is finished. Note that in this study of the dependency on collisionality, the collision frequency varies by a factor of 10^5 and the needed minimum simulation time also varies significantly since several (~ 10) collisional periods are needed to reach the saturated state of the fluxes and the current. The lowest collisional case is the most expensive one in order to observe reasonable results.
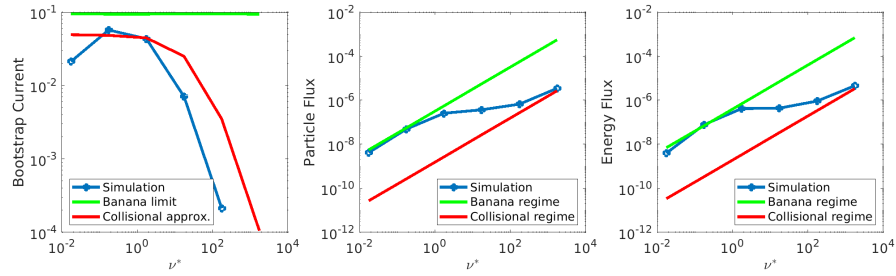
FIGURE 4.20: The maximum value of the particle flux, energy flux, and the bootstrap current for different values of collision frequency, taken at radial location $r = 0.23$. The blue lines represent the simulation result, while the green and red lines represent the analytical solutions.

4.4 Electron transport results for the moderate aspect ratio case

In addition to the large aspect ratio case $(a/R_0 = 1/10)$ in the previous section, in this section, we study the electron transport for the moderate aspect ratio case featured by $a/R_0 = 0.36$. The details of the magnetic equilibrium and the density profile are listed in the reference [24] and the main parameters are briefly summarized as follows. The major radius and the minor radius are $R_0 = 1.67$ m and $a = 0.6012$ m, respectively. In generating the EQDSK file as the input of the magnetic equilibrium, the $\bar{q}$ profile in Equation 4.2 is adopted with

$$\bar{q}(r_c) = 1.41 \quad , \quad \frac{r}{\bar{q}} \frac{d\bar{q}}{dr}(r_c) = 0.8369 \quad , \tag{4.6}$$

where $r_c = 0.5a$. The safety factor profile is shown in Figure 4.21.
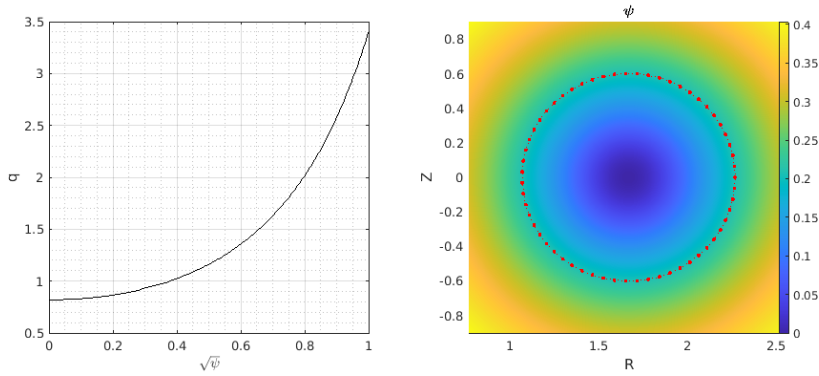
FIGURE 4.21: The q profiles (left) and poloidal magnetic flux map (right) of the cyclone case at moderate aspect ratio.

The radial profile of the density and its gradient are given analytically as follows [24],

$$n(r) = \exp\left\{-\kappa_n W_n \frac{a}{L_{ref}} \tanh\left(\frac{r-r_c}{W_A a}\right)\right\}; \tag{4.7}$$

$$\frac{d\ln n}{dr} = -\frac{1}{L_{ref}}\kappa_n \cosh^{-2}\left(\frac{r-r_c}{W_A a}\right); \tag{4.8}$$

where $L_{ref} = R_0$, $W_n = 0.3$, $\kappa_n = 2.23$. The density profile and its derivative used as the inputs of the simulations are shown in Figure 4.22. For the sake of simplicity, a uniform temperature profile is adopted.

Compared with the ITPA case $(R_0/a = 10, q \approx 1.75$ at $r/a = 0.5)$ studied in Chapter 4.3, the aspect ratio of the Cyclone case is smaller $(a/R_0 = 0.36)$. In addition, the safety factor is smaller than that of the ITPA case in the
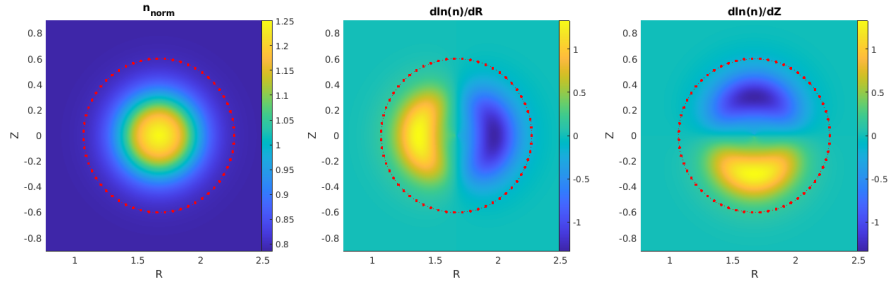
FIGURE 4.22: The density profiles for the cyclone moderate aspect ratio case.

inner radial region ($r < 0.5a$) but is larger near the edge. In the theoretical derivation, the small parameter $\rho_p = (qR_0/r)m_s v_\perp/(Z_s eB)$ is adopted as the expansion parameter, where Z_s is the charge number, and the subscript 's' indicates species 's'. As a result, for different values of q and r/R_0, the accuracy of the theoretical result can be different, which is more relevant for ion transport. As ρ_p is close to or even larger than the characteristic length of the equilibrium or/and the density/temperature profiles, the traditional neoclassical formulae are not valid and corrections are needed as shown in previous studies of ion transport [3, 11]. For electron transport, $\rho_p \ll 1$ is usually well satisfied except if it is very close to the magnetic axis where $R_0/r \to \infty$ and the traditional theoretical formulae can also break down.

In our simulation, we observe changes in the density of the order of 0.01% in the low collision frequency case, and about 2% in the high collisional case. We also observe large density changes on the axis, which can be due to the high density in the center and the enhanced particle density due to finite orbit width in simulation starting from Maxwellian distributions.
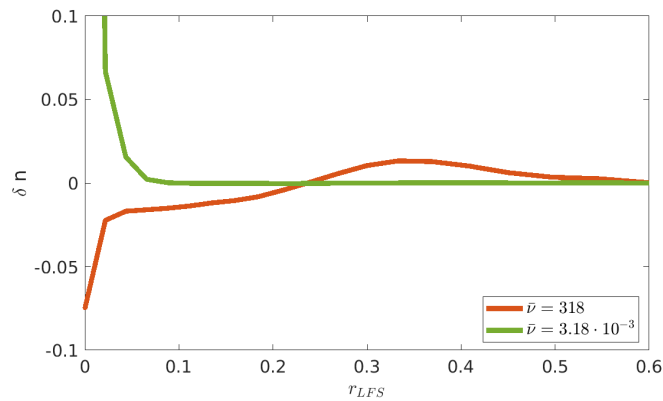

FIGURE 4.23: The radial profiles of the density change at the end of the simulation.

We again start by analyzing the radial particle flux, energy flux, and bootstrap current profiles of high and low collision frequency cases, as shown in Figures

4.24–4.25. For the low collisionality case, the agreement is not as good as that in the ITPA large aspect ratio case. The reason can be the large aspect ratio approximation adopted in the analytical formulas and the different treatments in our code for the poloidal-angle dependent values such as q in calculating the theoretical fluxes and the current. Specifically, when calculating the theoretical values of the fluxes and current, we calculate the theoretical values on numerous points in one annulus; then the averaged value is calculated with proper weights and thus the flux surface average value is obtained using the Monte-Carlo integration. This method of calculating the flux-surface-averaged fluxes and current gives us a convenient and practical way of calculating the fluxes and current for shaped tokamak geometry, as we also adopted for the ASDEX-Upgrade case in the next section. For the high collision frequency case, the agreement is better closer to the axis, which is also expected as the aspect ratio is larger. The bootstrap current is larger than the analytical solution and has a somewhat different shape for high collisions. The reason can be the approximation in the interpolation formula Equation 3.37, which is derived to match the results at the low and high collision regime. Indeed, theoretically, the discrepancies between the transition formula and the formulae at the low and high collisions are also observed theoretically [12], as shown in Figure 2.5. In the theoretical solutions, the interpolation formula is obtained by fitting the analytical results in the banana-plateau and plateau-collisional regimes, hence our simulation result is expected to be more exact than the analytical solution close to the plateau regime.
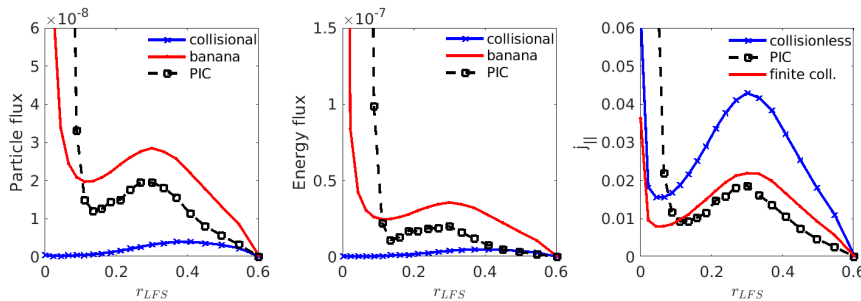

FIGURE 4.24: The radial profiles of the particle flux, energy flux, and the bootstrap current for the low collision frequency case, where $\bar{\nu} \approx 3 \cdot 10^{-3}$.

Analyzing how fluxes change with different collision frequencies, we take the radial location close to the maximum value of the fluxes ($r = 0.21$), which in this case is also a larger aspect ratio case. We observe good agreement with the analytical results for the particle and energy fluxes, as shown in Figure 4.26. The bootstrap current from the simulation follows the interpolation formula (red line) well. For $\nu^* > 10^2$, the discrepancy between the simulation and the interpolation formula is larger and it can be due to the high noise level in the simulations. In future investigations this case can be re-run with larger particle number. However, the current simulation uses 14 hours of computation time on
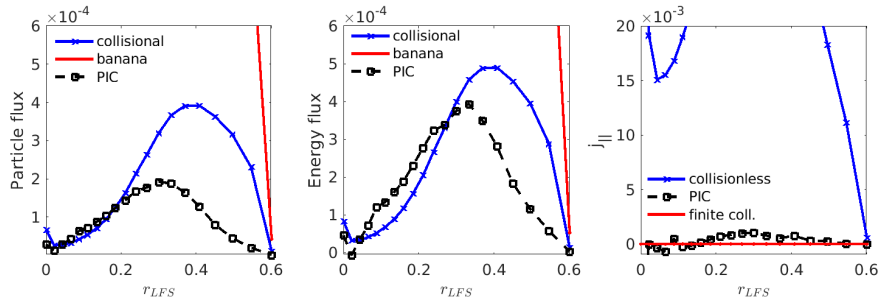
FIGURE 4.25: The radial profiles of the particle flux, energy flux, and the bootstrap current for the high collision frequency case, where $\bar{\nu} \approx 3 \cdot 10^2$.

4 nodes with each node containing two Intel(R) Xeon(R) Gold 6130 processors (16 cores per processor, 2.10GHz, 22MB Cache), as the bootstrap current is small in the high collision frequency limit further computationally intensive simulations were not run. Both the simulation results and the theoretical interpolation formula results are lower than the collisionless approximation and have the expected behavior of decreased value when the collision frequency is increasing.
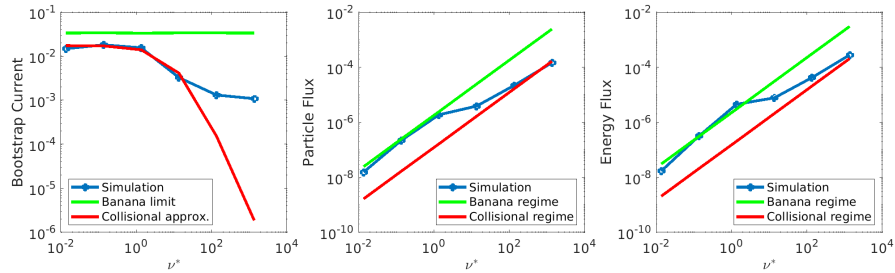
FIGURE 4.26: The values of the particle flux, energy flux, and the bootstrap current for $r_{LFS} = 0.21$ and different values of collision frequency. The blue lines represent the simulation result, while the green and red lines represent the analytical solutions.

4.5 Electron transport results for the ASDEX-Upgrade case

In this section, a realistic geometry for a Tokamak plasmas is used. The ASDEX Upgrade (AUG) case with shot number 34924 at 3.600 s is chosen as adopted by the previous work for the development of the TRIMEG code for the studies of the ion temperature gradient mode [24]. This is a typical discharge for the study of energetic particles and turbulence physics [18]. The EQDSK file is obtained from experimental data. The q profile and the poloidal magnetic flux function are shown in Fig. 4.27. In the simulation, we use the experimental equilibrium but the analytical density and temperature profiles in Equation 4.7, with the radial coordinate replaced with $\rho_{pol} = \sqrt{(\psi - \psi_0)/(\psi_b - \psi_0)}$, where the subscript 0 and b indicate the values at the magnetic axis and the last closed surface, respectively. In this work, we focus on testing the capability of the code in treating realistic geometry with minimum technical complexity. The density and the temperature profiles are shown in Fig. 4.28.
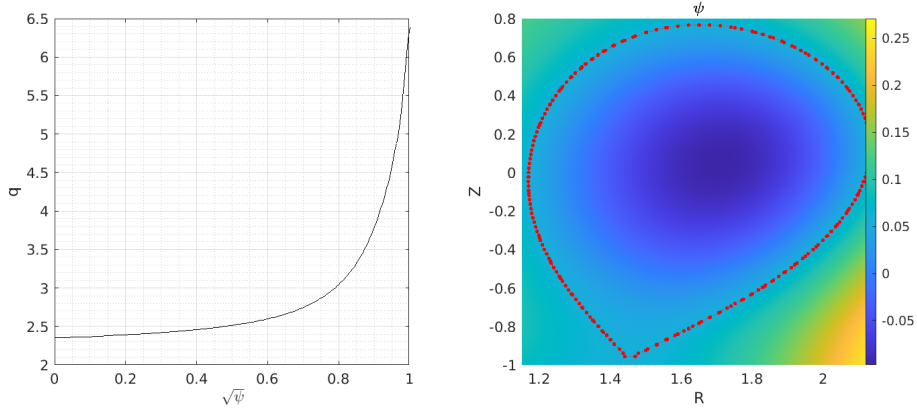

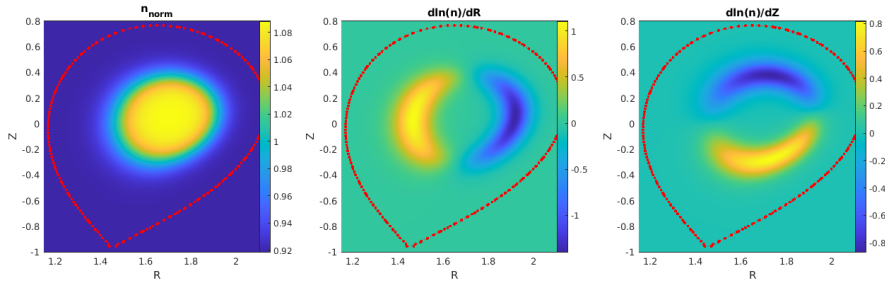FIGURE 4.27: The q profiles (left) and poloidal magnetic flux map (right) of the AUG case.

FIGURE 4.28: The density profiles for the AUG case.

As in previous chapters, we first look at the density changes due to low and

high collision frequencies as shown in Figure 4.29. We observe much lower density changes than in the previous cases. The density change due to high collision frequency is 0.6%, while in the low collision frequency case, it is almost negligible.
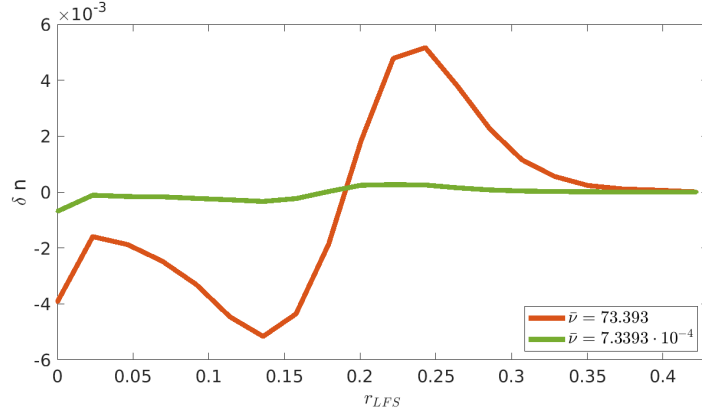

FIGURE 4.29: The radial profiles of the density change at the end of the simulation, where r_{LFS} indicates the radial coordinate from the axis to the low field side.

Looking at the radial profile for the low collision case given in Figure 4.30, we observe agreement with the theory. However, we also see issues with the simulation, where some values have become non-physical. For the low collision simulations, particle trajectories are calculated in a longer time scale than that in the collisional case, which requires dedicated treatment of the particle loss-refilling at the boundary and the control of numerical exceptions/errors. To make conclusions, the treatment of the geometry needs further investigation for long-time simulation in the low collision regime. As for the high collision frequency case, given in Figure 4.31, the discrepancy between theory and simulation is larger than that in the ITPA and Cyclone cases. In addition to the reason we discussed in the Cyclone case, for the AUG case, the magnetic flux surfaces are not circular but are strongly shaped. The theoretical formulae of fluxes and bootstrap current were derived for the circular magnetic flux surface originally [12] and our scheme of flux surface average of the fluxes and current is one possible way of an estimate which is more reasonable for circular magnetic flux surfaces and is for the verification of the implementation of the code. More accurate theoretical/numerical solutions for shaped tokamak plasmas can be found elsewhere [28, 1] and the comparison with our simulation results is possible but is beyond the scope of this work.

Furthermore, to investigate the dependence on the collision frequency we picked the radial coordinate where the highest values of fluxes were observed $(r_{LFS} = 0.2)$, and compared the analytical and simulation results, as shown in Figure 4.32. The agreement with the theory can still be seen. However, the agreement for large collision frequencies has gotten worse. Nevertheless, the trends of the fluxes and bootstrap current follow the theoretical results. More
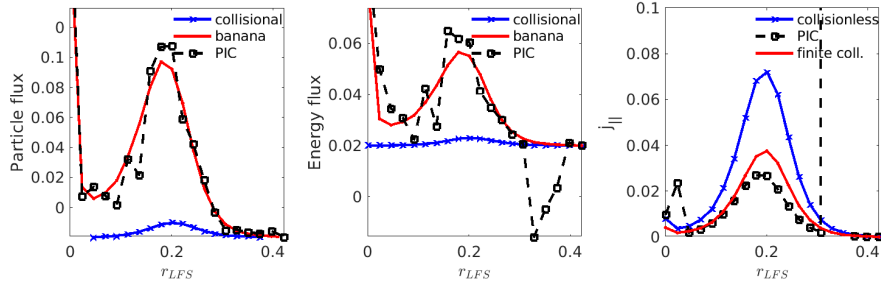
FIGURE 4.30: The radial profiles of the particle flux, energy flux, and the bootstrap current for the low collision case, where $\bar{\nu} \approx 7 \cdot 10^{-3}$.
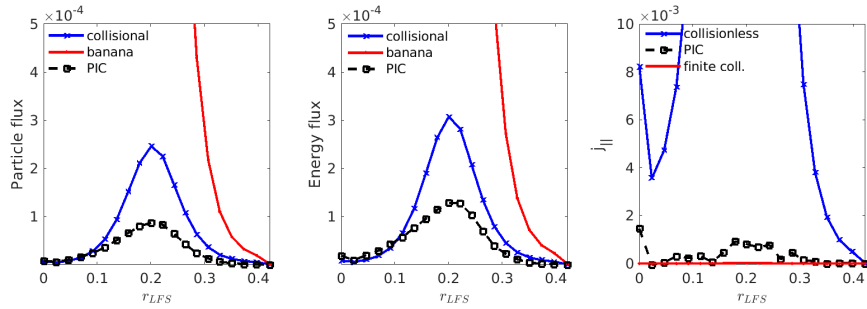

FIGURE 4.31: The radial profiles of the particle flux, energy flux, and the bootstrap current for the high collision case, where $\bar{\nu} \approx 7 \cdot 10^{1}$.

issues need to be studied for understanding the connections and the differences between the global gyro-kinetic simulation and the local theory, in order to identify the origin of the differences between the theoretical results and the simulation results.

Overall, comparing the three cases AUG and Cyclone cases showed most differences from the theoretical results while ITPA case was closest to the analytical solutions, as would be expected due to the large aspect ratio limit used during the derivation of the theoretical values. The AUG case requires further studies to investigate the limitations introduced by the realistic geometry. The agreement between the bootstrap current and the simulation for the lowest values of collision frequency could also be improved by increasing the simulation time, as currently all simulations were running on average for 16-32 hours using the computational resources described above.
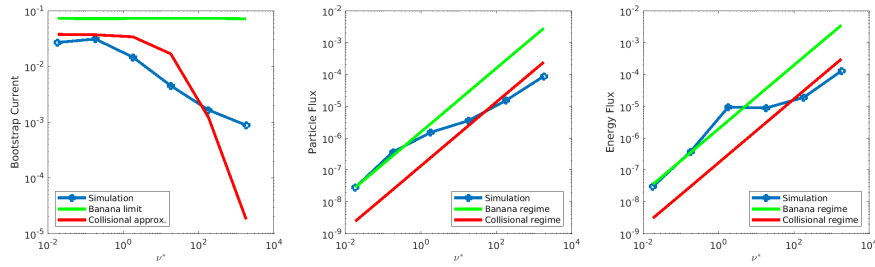
FIGURE 4.32: The values of the particle flux, energy flux, and the bootstrap current for different values of collision frequency at the low field side radius $r_{LFS} = 0.2$. The blue lines represent the simulation result, while the green and red lines represent the analytical solutions.

Chapter 5

Conclusion

The collision-induced neoclassical transport determines the minimum level of transport in tokamak plasmas. The generation of the neoclassical radial electric field plays a key role in the instability stabilization and the optimization of the confinement performance and the neoclassical bootstrap current can provide drive for instabilities. In this work, the collision operator and the electron neoclassical transport were studied theoretically and numerically.

Furthermore, the general form of the collision operator has been reviewed. Its reduction from the general form to the linearized form has been summarized, with a discussion on the conservation properties. For the electron transport and bootstrap current generation, we have added the pitch angle scattering operator to the TRIMEG code. Necessary diagnostic tools are implemented for the measurement of the particle/energy fluxes and the bootstrap current. The theoretical formulae are also implemented in the TRIMEG code.

We analyzed the electron transport and bootstrap current generation for three different cases. We considered a large aspect ratio ITPA case, a moderate aspect ratio Cyclone case, and a realistic AUG case. We simplified the model, by only considering the electron species, setting the temperature gradient to zero, and only taking into account the density gradients.

We started with a local model, which only simulated an annulus and got a good agreement with previous results from literature [21, 12]. We analyzed the convergence conditions for the code and made sure the parameters we set were giving physical results. For the large aspect ratio cases, we have found good agreement between theory and analytical solutions for the particle flux and the energy flux, while for the small aspect ratio, the agreement was worse. This was however expected, as the analytical results were obtained for the large aspect ratio approximation. For the bootstrap current, the agreement was good for low collision frequencies but then the magnitude of the current was much lower than expected from the analytical solutions. As these analytical solutions were interpolation formulae fitted from the two limits, an exact agreement was not

expected. However, better verification of the results and the identification of the limitations of the interpolation formulae require further investigation in a broader parameter regime.

In realistic AUG geometry, good numerical behaviors such as the convergence of the radial profiles are observed in bootstrap current and the fluxes in the collisional regime. Meanwhile, we found limitations in the flux calculations in the banana regime that need to be verified to have confidence in the results related to the low collision frequency case. However, regardless of this limitation, the agreement between the theory and the results was still good, and for higher collision frequencies, the energy and particle fluxes decreased in magnitude faster than the analytical solutions as the collision frequency increased.

The particle simulation of the neoclassical transport with the implementation of the collision operator provides a robust tool in a broad collisionality regime and for flexible parameters such as tokamak geometry. Future steps for further investigation would be to investigate the limitations related to the AUG geometry, especially in the banana regime. It also merits more efforts to add like-particle collision operators to also take into account ions in the simulation. After which, the particle-field coupling must be done, and the study of the radial electric field would be possible.

Bibliography

[1]   EA Belli and J Candy. "Kinetic calculation of neoclassical transport including self-consistent electron and impurity dynamics". In: *Plasma Physics and Controlled Fusion* 50.9 (2008), p. 095010.

[2]   AJ Brizard and TS Hahm. "Foundations of nonlinear gyrokinetic theory". In: *Reviews of modern physics* 79.2 (2007), p. 421.

[3]   CS Chang and FL Hinton. "Effect of finite aspect ratio on the neoclassical ion thermal conductivity in the banana regime". In: *The Physics of Fluids* 25.9 (1982), pp. 1493–1494.

[4]   CS Chang, S Ku, and H Weitzner. "Numerical study of neoclassical plasma pedestal in a tokamak geometry". In: *Physics of Plasmas* 11.5 (2004), pp. 2649–2667.

[5]   P Donnel et al. "Moment approach of the multi-species non-linear Coulomb collision operator adapted to particle-in-cell codes". In: *Plasma Physics and Controlled Fusion* 63.2 (2020), p. 025006.

[6]   A Fil. "Modélisation des disruptions déclenchées par injection massive de gaz dans les plasmas de tokamaks". PhD thesis. Sept. 2015.

[7]   R Fitzpatrick. *Plasma physics: an introduction.* Crc Press, 2014.

[8]   R.J. Goldston. *Introduction to Plasma Physics.* CRC Press, 2020. ISBN: 9781439822074.

[9]   R Hatzky et al. "Reduction of the statistical error in electromagnetic gyrokinetic particle-in-cell simulations". In: *Journal of Plasma Physics* 85.1 (2019).

[10]   R.D. Hazeltine and F.L. Waelbroeck. *The Framework of Plasma Physics.* Frontiers in Physics. Taylor & Francis Group, 2019. ISBN: 9780367314170.

[11]   P Helander. "Bifurcated neoclassical particle transport". In: *Physics of Plasmas* 5.11 (1998), pp. 3999–4004.

[12]   FL Hinton and RD Hazeltine. "Theory of plasma transport in toroidal confinement systems". In: *Reviews of Modern Physics* 48.2 (1976), p. 239.

[13]   GTA Huysmans and O Czarny. "MHD stability in X-point geometry: simulation of ELMs". In: *Nuclear fusion* 47.7 (2007), p. 659.

[14]   S Jardin. *Computational methods in plasma physics.* CRC press, 2010.

[15]   Axel Könies et al. "Benchmark of gyrokinetic, kinetic MHD and gyrofluid codes for the linear calculation of fast particle driven TAE dynamics". In: *Nuclear Fusion* 58.12 (2018), p. 126027.

[16]   E Lanti. *Global Flux-Driven Simulations of Ion Temperature-Gradient and Trapped-Electron Modes Driven Turbulence with an Improved Multithreaded Gyrokinetic PIC Code*. Tech. rep. EPFL, 2019.

[17]   LL Lao et al. "Reconstruction of current profile parameters and plasma shapes in tokamaks". In: *Nuclear fusion* 25.11 (1985), p. 1611.

[18]   PH Lauber et al. "Strongly non-linear energetic particle dynamics in ASDEX Upgrade scenarios with core impurity accumulation". In: *proceedings of the 27th IAEA Fusion energy* (2018).

[19]   Ph Lauber et al. "LIGKA: A linear gyrokinetic code for the description of background kinetic and fast particle effects on the MHD stability in tokamaks". In: *Journal of Computational Physics* 226.1 (2007), pp. 447–465.

[20]   S Li et al. "Optimal tracking for a divergent-type parabolic PDE system in current profile control". In: *Abstract and Applied Analysis*. Vol. 2014. Hindawi. 2014.

[21]   Z Lin. *Gyrokinetic particle simulations of neoclassical transport*. Princeton University, 1996.

[22]   Z Lin, WM Tang, and WW Lee. "Large orbit neoclassical transport". In: *Physics of Plasmas* 4.5 (1997), pp. 1707–1713.

[23]   RG Littlejohn. "Variational principles of guiding centre motion". In: *Journal of Plasma Physics* 29.1 (1983), pp. 111–125.

[24]   ZX Lu et al. "Development and testing of an unstructured mesh method for whole plasma gyrokinetic simulations in realistic tokamak geometry". In: *Physics of Plasmas* 26.12 (2019), p. 122503.

[25]   ZX Lu et al. "Full f and δf gyrokinetic particle simulations of Alfvén waves and energetic particle physics". In: *arXiv preprint arXiv:2210.04354* (2022).

[26]   ZX Lu et al. "The development of an implicit full f method for electromagnetic particle simulations of Alfvén waves and energetic particle physics". In: *Journal of Computational Physics* 440 (2021), p. 110384.

[27]   MN. Rosenbluth, WM. MacDonald, and DL. Judd. "Fokker-Planck Equation for an Inverse-Square Force". In: *Phys. Rev.* 107 (1 July 1957), pp. 1–6. DOI: 10.1103/PhysRev.107.1.

[28]   O Sauter, C Angioni, and YR Lin-Liu. "Neoclassical conductivity and bootstrap current formulas for general axisymmetric equilibria and arbitrary collisionality regime". In: *Physics of Plasmas* 6.7 (1999), pp. 2834–2839.

[29]   E Sonnendrücker. *Lecture notes in Computational plasma physics*. Technical University of Munich, 2022. URL: https://www-m16.ma.tum.de/Allgemeines/CompPlasmaPhys.

[30]   W Tang. *General plasma physics 2, Lecture Notes*. 2009.

[31]   T Vernay et al. "Collisional Electrostatic Simulations of Turbulence with the Global Gyrokinetic Code ORB5". In: *14th European Fusion Theory Conference*.

[32] WX Wang et al. "Gyro-kinetic simulation of global turbulent transport properties in tokamak experiments". In: *Physics of Plasmas* 13.9 (2006), p. 092505.

[33] J Wesson and DJ Campbell. *Tokamaks*. Vol. 149. Oxford university press, 2011.

[34] RB White. *Theory Of Toroidally Confined Plasmas*. World Scientific Publishing Company, 2013.

[35] XQ Xu and MN Rosenbluth. "Numerical simulation of ion-temperature-gradient-driven modes". In: *Physics of Fluids B: Plasma Physics* 3.3 (1991), pp. 627–643.

Acknowledgements